Mapping the physico-chemical properties of mineral dust in Western Africa: Mineralogical composition

P. Formenti[1], S. Caquineau[2], K. Desboeufs[1], A. Klaver[1], S. Chevaillier[1], E. Journet[1], and J. L. Rajot[1,3]

[1] LISA, UMR CNRS 7583, Université Paris Est Créteil et Université Paris Diderot, Institut Pierre Simon Laplace, Créteil, France

[2] IPSL/LOCEAN, UMR 7159 - IRD-CNRS-UPMC-MNHN, Institut de Recherche pour le Développement, Bondy, France

[3] IEES, UMR IRD 242 – IRD – UPMC – CNRS – UPEC - AgroParisTech, Bondy, France

Abstract

In the last few years, several ground-based and airborne field campaigns have allowed exploring the properties and impacts of mineral dust in Western Africa, one of the major emission and transport areas worldwide. In this paper, we explore the synthesis of these observations to provide with a large-scale quantitative view of the mineralogical composition and its variability with source region and time after transport.

This work reveals that mineral dust in Western Africa is a mixture of clays, quartz, iron and titanium oxides, representing at least 92% of the dust mass. Calcite ranged between 0.3 and 8.4% of the dust mass depending on the origin. Our data do not show a systematic dependence of the dust mineralogical composition with origin, likely as in most of the cases they represent the composition of the atmospheric burden after 1–2 days after emission, when air masses mix and give raise to a more uniform dust load. This has implications for the representation of the mineral dust composition in regional and global circulation models, and satellite retrievals.

Iron oxides account for 58 ± 7% of the mass of elemental Fe, and between 2 and 5% of the dust mass. Most of them are composed of goethite, representing between 52 and 78% of the iron oxide mass. We estimate that titanium oxides account for 1-2% of the dust mass, depending on whether the dust is of Saharan or Sahelian origin.

The mineralogical composition is a critical parameter to estimate the radiative and biogeochemical impact of mineral dust. The results on dust composition have been applied to estimate the optical properties as so as the iron fractional solubility of Saharan and Sahelian dust.

Data presented in this paper are provided in numerical form upon email request while they are being implemented as a public database, the Dust-Mapped Archived Properties (DUST-MAP), an open repository for compositional data from other source regions in Africa and worldwide.

1. Introduction

Mineral dust from wind-driven soil erosion is an important player in the climate system. It is emitted in large quantities from arid and semi-arid regions of the globe, mostly Africa, Asia, Australia and North America (Shao et al., 2011), accounting for about 2000 Mt to the annual aerosol emissions at the global scale. Once in the atmosphere, mineral dust has several climatic and environmental impacts, related to its ability of scattering and absorbing radiation, both in the solar and terrestrial spectra, of acting as giant cloud and ice nuclei, of altering the concentrations of some gaseous pollutants (such as ozone), and of providing nutrients to the ecosystems via dry and wet deposition, whereby also changing the surface albedo (Shao et al., 2011; Mahowald et al., 2011). The relevance of those phenomena can be expressed in terms of radiative forcing, whose magnitude, in terms of central values, is estimated to be as high as 0.5–1 W m^{-2} at the global scale (Mahowald et al., 2011).

However, uncertainties remain important, because of the spatial heterogeneity of concentrations, due to localized emission and short residence time in the atmosphere (1 week at the most, depending on particle size), but also because of the far from satisfactory knowledge on the underlying physico-chemical properties, composition, size and shape, ruling the optical, chemical and physical interactions of mineral dust with radiation and the atmospheric/terrestrial/oceanic constituents (Formenti et al., 2011a).

This is particularly the case of the composition. Dust is made of different minerals, whose proportions, at emission, depend on the mineralogy of the source region and surface wind speed relative to the soil roughness, which determines their size distribution (Marticorena and Bergametti, 1995, Alfaro et al. 1998). The various minerals, clays, quartz, potassic and sodic feldspars, calcium-rich carbonates and sulphates, iron and titanium oxides, have different mineralogical and crystallographic properties, therefore they may act differently with respect to light extinction, absorption of water, and surface reactivity (Pye, 1987). For example, iron oxides have been shown to control the interaction with light in the UV-visible spectrum (Sokolik and Toon, 1999), whereas quartz, clays and Ca-rich carbonates become important when looking at the infrared part of the radiation spectrum (Sokolik et al., 1998). Clays but also feldspars come to play when it comes in investigating the capacity of dust of activating as ice nuclei at low temperature (Hoose et al., 2008; Atkinson et al., 2013), whereas calcite (calcium carbonate) shows high surface reactivity with respect to various atmospheric pollutants (Crowley et al., 2010). Another clay family, the smectites, bears the

most soluble iron which might become available as nutrient to the marine phytoplankton (Journet et al., 2008). The properties of mineral dust are size-dependent, and the dimensional spectrum of mineral dust particles at emission extends over various orders of magnitude from approximately 200-300 nm to 100 μm (Kandler et al., 2009) depending on wind speed at emission. As a consequence, the properties of mineral dust vary as a function of time after emission due to size-dependent deposition, mixing, and gaseous condensation. Because these processes are not well established, the physico-chemical properties of mineral dust have to be determined experimentally at the various times of their life cycle.

In this paper, we relate on the mineralogical and chemical composition at emission or at most within 1–2 days from emission of mineral dust over Western Africa. The southern Sahara is the location of two of most persistent dust sources at the global scale, the Bodélé depression in between the Tibesti and the Ennedi mountain chains in Chad, and the areas in between the east of Mauritania, the North of Mali and the south of Algeria (Prospero et al., 2002; Laurent et al., 2008; Washington et al., 2006; Shao et al., 2011). These sources are relevant at the global scale as their emissions are transported across the Atlantic Ocean towards South and Central America (Reid et al., 2003; Koren et al., 2006; Ben-Ami et al., 2009; 2010).

The atmospheric content of mineral dust in Western Africa shows a very pronounced seasonal cycle despite high variability, both at the daily and inter-annual scales (N'Tchayi et al., 1994; N'Tchayi Mbourou et al., 1997; Goudie and Middleton, 2001). This is largely explained by the alternance of two meteorological regimes. Throughout the year, the "Harmattan", a north-eastern dry wind, is responsible for intense dust emissions in the arid areas of the Sahara and very efficient transport towards the Atlantic Ocean and across the Sahel (Pye, 1987; Sokolik et al., 2001; Laurent et al., 2008). Wintertime is also the biomass burning season south of approximately 13°N (Haywood et al., 2008), and mixing between dust and biomass burning aerosols might occur during southward transport (Johnson et al., 2008). During summer, the Inter Tropical Convergence Zone (ITCZ) displaces northward, allowing the surface Monsoon flow to intrude the continent from the South-West towards the continental Sahel. This shift induces a progressive organization of convection from isolated cells to large-scale fast propagating systems, which, particularly at the beginning of the Monsoon season, are often not precipitating, and efficient in eroding bare soils and producing mineral dust (Marticorena et al., 2010; Abdourhamane Touré et al., 2011). The summertime column dust content over western Africa results therefore from the superimposition of local emission from the Sahel and remote transport of dust emitted in the Sahara (Tegen and Fung, 1994; Yoshioka et al., 2005; Marticorena et al., 2010).

The mineralogy of the Saharan and Sahelian source areas have different mineralogy: the Sahara is mainly composed by calcisols or arenosols, whereas the Sahel is richer in weathered plinthosols (Fe oxides/kaolinite/quartz) (Pye, 1987; Claquin et al., 1999; Caquineau et al., 2002; Nickovic et al., 2012; Journet et al., 2014). As a consequence, mixing or layering of dust transported from the Sahara and locally emitted by convection over the Sahel should be detectable through differences in the composition over the atmospheric column.

Furthermore, western Africa is prone to land-use change because of the rapid demographic increase and desertification during drought periods (ECA, 2005; Dai, 2011), which could feedback in increased emission (Carslaw et al., 2010). Rajot (2001) have shown that, in the Sahel, additional emission by wind erosion of mesoscale meteorological disturbances, such as organized convective systems, occurs on harvested soils only. These additional emissions, anthropogenic in origin, are not quantified to date (Boucher et al., 2013).

To provide with the quantitative estimate of the mineralogical composition of mineral dust at the regional scale, we report in this paper the synthesis of data from various aircraft and ground-based field campaigns which have taken place in western Africa in 2006 and 2007. These are the African Monsoon Multidisciplinary Analysis (AMMA) Special Observing Period-0 (SOP0; Rajot et al., 2008), augmented of the airborne Dust and Biomass-burning Experiment (DABEX; Haywood et al., 2008), and Special Observing Period-1 and -2 (SOP1-2; Reeves et al., 2010); the Dust Outflow and Deposition to the Ocean (DODO; McConnell et al., 2008) and the Geostationary Earth Radiation Budget Intercomparison of Longwave and Shortwave radiation (GERBILS; Haywood et al., 2011).

Some of the data discussed in this paper have been published previously (Formenti et al., 2008; 2011b; Rajot et al., 2008; Klaver et al., 2011). Here, they are revisited with a broader perspective discussion of the mineralogical variability at the regional scale of Western Africa and its implications for climate.

This paper discusses whether, when mapped at the scale of western Africa, the regional variability at emission deriving from the heterogeneity of the mineralogy of the parent soils is still relevant or whether it becomes irrelevant when dust is airborne. This is important for developing a model parameterisation for dust in regional and global climate models or for satellite retrieval algorithms.

2. Methods

Full details of the field campaigns operations, experimental procedures, collection and analytical protocols are described in a number of companion papers (Hawyood et al., 2008;

2011; Formenti et al., 2008; 2011b; Rajot et al., 2008; McConnell et al., 2008; 2010; Klaver et al., 2011) which are resumed hereafter.

2.1. Field campaigns

The African Monsoon Multidisciplinary Analysis (AMMA) was an international project to improve our knowledge and understanding of the West African monsoon (WAM), its variability on daily-to-interannual time scales, and its effects on the status of the atmosphere (Redelsperger et al., 2006). Because of its links to precipitation, wind speed, soil surface state, and drought at different time scales, mineral dust aerosols play a role in this comprehensive scientific framework.

The experimental strategy of the AMMA program was based on embedded multi-year, seasonal and intensive observation periods (Janicot et al., 2008; Lebel et al., 2010). The observations used in this paper were conducted during the intensive observations periods, called Special Observing Periods (SOPs). The wintertime SOP (SOP0), was dedicated to the investigation of mineral dust and biomass burning, and their mixing, took place from 13 January and 13 February 2006. The summertime observations (periods SOP1 and SOP2) started on 31 May 2006 and ended on 17 July 2006 and were dedicated to the fine description of the interactions between aerosols and convection.

The ground-based observations were conducted at the AMMA supersite of Banizoumbou (13.5°N; 2.6°E, 250 m above sea level), located at a remote location at about 60 km east from the capital of Niger, Niamey. This site has been operational since the early 1990s, when the first measurements of soil erosion were performed on a cultivated field and a fallow (Rajot, 2001). Since 1995, the site is also an Aerosol Robotic Network (AERONET) station measuring columnar aerosol optical properties. The ground-based site operations are fully described in Rajot et al. (2008).

The aircraft observations were conducted from Niamey, Niger. The wintertime airborne campaign, called AMMA SOP0-DABEX, was conducted onboard the Facility for Airborne Atmospheric Measurements (FAAM) BAe-146 aircraft (Haywood et al., 2008). The aircraft performed thirteen research flights in the area between 8°N and 18°N, including three dedicated excursion to the north of Niger, toward the Aïr Mountains and the Ténéré desert to probe specifically mineral dust whilst transport. In summertime, the observations were conducted onboard the Service des Avions Français Instruments pour la Recherche en Environnement (SAFIRE) ATR-42, which operated twenty research flights in the area between 6° and 20°N, therefore crossing the ITCZ to the north to contrast the Sahara and the Sahelian dust properties in their respective boundary layers (Reeves et al., 2010; Formenti et al., 2011b).

The Geostationary Earth Radiation Budget Intercomparison of Longwave and Shortwave radiation (GERBILS) found its scientific motivation in the discrepancy that had been found between the satellite observations and the numerical weather model predictions of the top of the atmosphere outgoing longwave radiation over desert areas in western Africa (Haywood et al., 2005). This discrepancy could be reconciled by including mineral dust in the model. The GERBILS experiment, whose full rationale and operating details are described in Haywood et al. (2011), was therefore designed to test this hypothesis, and to determine the properties of the mineral dust to be included in the model. The experiment consisted in ten research flights onboard the FAAM BAe-146 performed between Nouakchott (18.10°N, 15.94°W, Mauritania) and Niamey (13.48°N, 2.18°E, Niger) on an almost standard route along the 18°N meridian. Flights were performed between 18 and 29 June 2007, in a period characterised by a persistent and widespread dust load.

Finally, the Dust Outflow and Deposition to the Ocean (DODO) airborne experiment took place at two different periods in 2006: in wintertime (7–16 February) and in summertime (22–28 August). The aim of DODO was to characterised dust as a possible nutrient for the marine ecosystems. For this reason, the FAAM BAe-146 aircraft was based in Dakar, in Senegal, and most of the twelve research flights (six in the winter period and six in the summer period, respectively) were conducted over the Atlantic Ocean in the outflow from the African continent. However, two flights, one per season, were performed inland above Mauritania in order to sample dust at or very close after emission (McConnell et al., 2008).

2.2. Sample collection and handling

2.2.1. Ground-based

Aerosol sampling at the ground-based AMMA super site of Banizoumbou was performed using two identical purpose-built wind-oriented inlets designed for the AMMA field campaigns (Rajot et al., 2008). The cut-off diameter 50% efficiency of these inlets has been calculated to be approximately 40 μm by using the standard formulae of particle losses in inlets and tubings reported in Baron and Willeke (2001) and Hinds (1999). Each inlet leads to a sampling chamber containing seven different sampling lines, each of them dedicated to a different instrument. Multiple sampling lines are very convenient as they allow collecting various filter samples in parallel, differentiated and optimized in terms of sampling medium, exposure interval and flow rate as a function of the analytical technique to be applied. This also results in minimal manipulation of the filters after sampling. Samples were collected on acid washed 42-mm polycarbonate Nuclepore filters (0.4 μm pore size) mounted on plastic rings. Samples were stored in Petri dishes after sampling. Sampling time was of the order of hours, and was varied depending on the aerosol mass concentration measured on-line by a

211 Tapered Element Oscillating Microbalance (TEOM, Rupprecht and Patashnick, Albany, USA)
212 (Rajot et al., 2008).

213 **2.2.2. Airborne**

214 During the AMMA SOP0-DABEX, DODO and GERBILS campaigns, samples were collected
215 onboard the FAAM BAe-146 aircraft. The aircraft is capable of carrying 2 crew, 18 scientists
216 and a total scientific payload of up to 4000 kg for a distance of 3700 km with a ceiling of
217 35,000 feet and has a typical science speed of 110 m s^{-1}. For the typical scientific payload,
218 flight patterns, ambient meteorological conditions and the proximity of diversion airports
219 encountered during the campaigns, the average endurance of the BAe146 aircraft was
220 approximately 5 hours. Sampling was been performed using a set of two parallel thin-walled
221 inlet nozzles with a curved leading edge; the design was based on criteria for aircraft engine
222 intakes at low Mach numbers (Andreae et al., 1988). The sampling system was operated at
223 flow rates that averaged at 120 L min^{-1} (at ambient pressure and temperature; the flow was
224 adjusted to maintain slightly subisokinetic sampling conditions. The passing efficiency of the
225 inlets has not been formally quantified. During AMMA SOP-0/DABEX, Chou et al. (2008)
226 showed that the number size distributions of the aerosols collected on the filters (counted by
227 electron microscopy) extended up to 10 µm diameters and were of comparable magnitude to
228 those measured by wing-mounted optical counters.

229 Aerosol particles were sampled by filtration onto two stacked-filter units (SFUs) mounted in
230 parallel. Each SFU can hold a maximum of three filters on sequential 47- or 90-mm diameter
231 polyethylene supports. Only one stage was used during the campaigns, i.e., samples
232 represented the aerosol bulk composition. Samples were collected only during horizontal
233 flight legs lasting not less than 20 min in order to guarantee sufficient loading of the filter
234 samples. As a consequence, at the aircraft cruise speed, each sample had at best a spatial
235 resolution of 180 km. Each SFU consisted of a Nuclepore filter (Whatman) of nominal pore
236 size 0.4 µm.

237 During the AMMA SOP1-2 campaigns, samples have been collected onboard the SAFIRE
238 ATR-42. With the necessary payload for the campaign, the aircraft had a maximum
239 endurance of 4 h. Minimum flight altitude is 300 m over land. Ceiling is approximately 7 km.
240 The aircraft was equipped with basic sensors for measuring the radiative, dynamic and
241 thermodynamic properties of the atmosphere (Saïd et al., 2010).

242 Aerosol sampling was performed using the AVIRAD aerosol sampling system newly
243 developed for AMMA (Formenti et al., 2011b). It consists of an iso-axial and isokinetic inlet
244 whose 50% passing efficiency has been estimated at 9 µm in diameter. At the cruise speed
245 of the ATR-42 (93 m s^{-1}) the delivered volumetric flow rate is 350 L min^{-1}, which was

distributed to various instruments, including two SFU for collecting bulk aerosol samples. Samples were obtained by parallel filtration onto 42-mm diameter polycarbonate membranes (nominal pore size 0.4 µm Nucleopore, Whatman) on polyethylene supports. Samples were collected only during horizontal flight legs lasting not less than 20 minutes. Immediately after each flight, the loaded filters were stored in Petri dishes.

Ground-based operation with multiple sampling lines allowed for parallel sampling where the sampling duration is adapted to the characteristics (detection limit, saturation level) of the technique to be employed for analysis. On aircraft, the two parallel samples available had to be manipulated further to allow accommodating the number of analysis one wanted to perform, also taking into account the fact that some analyses are destructive of the sample. Therefore, the handling protocol for aircraft samples consisted in analysing entire filters or portions of those depending on their load on mineral dust. A dedicated tool in polyethylene has been developed for cutting the 47- or 90-mm filters into halves, quarters or eighth without touching and therefore contaminating them.

2.3. Sample analysis

2.3.1. Elemental composition

The total elemental concentrations for elements from Na to Pb by wavelength dispersive X-ray fluorescence (WD-XRF) for samples collected on the ground and on the ATR-42 and Particle-Induced X-ray Emission (PIXE) for the aircraft samples collected onboard the BAe-146. The reason for using different techniques for ground-based and aircraft samples lays on the fact that the WD-XRF sample holder set up could not, at the time, host filters which are not supported on polyethylene frames. The details of the analytical protocols are provided in Formenti et al. (2008; 2011b), McConnell et al. (2008), Rajot et al. (2008) and Klaver et al. (2011). Elemental concentrations are estimated with a 5% error. An inter-comparison exercise on samples generated in the laboratory from geo-standards of known and certified composition has shown that the two techniques yield comparable results within the error bars (Formenti et al., 2010).

2.3.2. Mineralogical composition

The identification of major minerals composing mineral dust: quartz (SiO_2), calcite ($CaCO_3$), dolomite ($CaMg(CO_3)_2$, gypsum ($CaSO_4 \cdot 2H_2O$), clays (kaolinite, illite, smectite, chlorite), feldspars (ortoclase $KAlSi_3O_8$ and albite $NaAlSi_3O_8$) was performed by X-ray diffraction (XRD) analysis at the Institut de Recherche pour le Développement (IRD) in Bondy, France. The diffractometer, a Siemens D500 with Ni-filtered Cu-Kα radiation, was operated at 40 kV and 30mA. Samples were scanned from 2 to 70° (2θ) with counting for 10 s every 0.02° (2θ). The analytical procedure and semi-quantitative treatment are fully described by Caquineau et

al. (1997), who adapted the sample preparation to low-mass mineral aerosol (load deposited on filter > 800 µg). The calibration protocol that was applied to the XRD spectrometer in order to quantify the mineralogical composition is described in Klaver et al. (2011). An improvement of the calibration curves was performed after publication of the Klaver et al. (2011) paper by achieving the calibration for the feldspars (ortoclase and albite). The calibration factors K_i representing the ratio between the peak surface area S_i in the diffraction spectra and the mass m_i of the i-mineral are reported in Table 1. The error on the mineral masses is estimated as the sum of the relative error on the peak area in the diffractograms and on the calibration factor K_i as $\frac{\Delta m_i}{m_i} = \frac{\Delta K_i}{K_i} + \frac{\Delta S_i}{S_i}$. The term $\Delta K_i/K_i$ is estimated from the error of the slope of the calibration curve (Table 1) and it varies between 2% and 10%. The term $\Delta S_i/S_i$ depends on the abundance of the mineral in the samples and has been estimated from the obtained counting statistics.

2.3.3. Iron oxide content and speciation

The iron oxide content, defined as the fraction of iron which is not in the crystal lattice of silicates (Karickhoff and Bailey, 1973), was determined with the adapted Citrate-Bicarbonate-Dithionite (CBD) extraction method developed by Lafon et al. (2004). This method is an adaptation for aerosol filters (with typical material mass less than 500 µg) of the classical method of (Mehra and Jackson, 1960) for soil analysis. The method uses a reagent to dissolve iron oxides selectively via reduction. Details of this analysis are given in Formenti et al. (2008; 2011b) and Klaver et al. (2011). The percent error on the iron oxide content is estimated to be 10% as its assessment is based on two XRF analysis (prior and after dissolution of the iron oxides from the sample).

The speciation of iron oxides was performed by X-ray absorption (XAS) at the Fe K-range: XANES (X-ray Absorption Near Edge Structure) and EXAFS (Extended X-ray Absorption Fine Structure) at the SAMBA (Spectroscopies Applied to Materials based on Absorption, http://www.synchrotron-soleil.fr/portal/page/portal/Recherche/LignesLumiere/SAMBA) line SOLEIL synchrotron facility in Saclay, France. XAS spectroscopy is based on the analysis of the position and shape of the K-pre-edge and edge peaks, depending on the oxidation state of iron but also to the atomic position of the neighbouring atoms, mostly O+ and OH-. The quantification of the Fe-status was based on the analysis of five standards of Fe(III)-bearing minerals which can be found in mineral dust. Full details of the experimental protocols and the data analysis are provided in *Formenti et al., Dominance of goethite over hematite in iron oxides of mineral dust from Western Africa: quantitative partitioning by X-ray Absorption Spectroscopy, submitted to J. Geophys. Res., 2014* (hereafter referred as Formenti et al., 2014).

2.4. Data interpretation and presentation

2.4.1. Source identification

The identification of source regions has been performed using a variety of ancillary products:

(1) The record of measurements of the horizontal movement of sand grains by a saltiphone (Eijkelkamp, Giesbeek, The Netherlands) located at the proximity of the sampling inlets at the super-site of Banizoumbou providing with the estimate of the saltation horizontal flux related to established local erosion (Sow et al., 2009).

(2) Various satellite products, in particular, the daily images of the UV aerosol index by the Ozone Monitoring Instrument (OMI) on Aura; the instantaneous dust product maps from the SEVIRI satellite; and the Infrared Difference Dust Index (IDDI) obtained from the infrared channel of Meteosat (10.5-12.5 μm) (Legrand et al., 1994).

(3) Back-trajectories and air mass dispersion calculations using the Met Office Numerical Atmospheric-dispersion Modeling Environment (NAME, Cullen, 1993) and the NOAA HYbrid Single-Particle Lagrangian Integrated Trajectory Model (HYSPLIT) as described in Chou et al. (2008), Rajot et al. (2008) and Klaver et al. (2011).

2.4.2. Data presentation

2.4.2.1. Calculation of the total mass

In the following, the composition of mineral dust will be presented as percent of the total dust mass (TDM). According to Pye (1987), the TDM can be decomposed as

$$TDM = m_{clays} + m_{quartz} + m_{Ca-rich} + m_{feldspars} + m_{iron\ oxides} + m_{tit\ oxides} + m_{organic} \quad (1)$$

where

m_{clays} = mass of the major clay-species (kaolinite, illite, smectite, chlorite)

m_{quartz} = mass due to quartz (SiO_2)

$m_{Ca\text{-}rich} = m_{calc} + m_{dolom} + m_{gypsum}$ = mass due to calcium carbonates and sulphates in the form of calcite ($CaCO_3$), dolomite ($CaMg(CO_3)_2$) and gypsum ($CaSO_4$)

$m_{feldspars}$ = mass due to feldspars, such as albite and ortoclase ($NaAlSi_3O_8$ and $KAlSi_3O_8$, respectively)

$m_{iron\ oxides}$ = mass due to hematite (α-Fe_2O_3) and goethite (α-FeOOH)

$m_{tit\ oxides}$ = mass due to titanium oxides (TiO_2)

$m_{organic}$ = mass due to organic matter which is present in the soils as biological debris and complex organic molecules (humus).

In practical terms, the TDM can be approximated by the TEDM (total estimated dust mass) as the sum of the oxide-equivalent of the elemental concentrations of the major elements in mineral dust (Al, Si, Fe, Ca, K, Ti accounted as Al_2O_3, SiO_2, Fe_2O_3, $CaCO_3$, K_2O and Ti_2O) whose masses are measured by XRF analysis. The TEDM estimated this way can be compared to the direct measurement of the total dry gravimetric mass (TDGM), which is available for some of the datasets (ground-based AMMA SOP0 and SOP1-2, and GERBILS), either by weighing or by on-line Tapering Element Oscillating Microbalance (TEOM, model 1400a, Rupprecht and Patashnick Albany, New York USA) (see Rajot et al. (2008) and Klaver et al. (2011)).

The slope of the least-squared linear regression between the TEDM and TDGM, calculated on the 81 samples on which the extraction of iron oxides was performed (see section 3.3), is 0.98 and the coefficient of determination (R^2) is 0.88. This is very satisfactory, taking into account that, because the mass is dominated by coarse particles, which have large mass but little number, differences might arise by losses of some coarse particles between the time at which the filter was weighed and the time at which it was analysed by XRF or by small differences between the filter sampling duration and the TEOM integration times. As a matter of fact, the most of the scatter in the data is observed for samples which corresponded to local erosion or transported emission by convective systems, having the largest fraction of coarse particles and the shortest integration times. This becomes apparent when plotting separately the ground-based AMMA SOP0 and SOP1-2 data (Figure 1).

Therefore, we consider that the TDM is equal to the TDGM for samples for which the TDGM is measured. When this is not available, the TDM is approximated via the TEDM calculated as sum of oxides. The percent uncertainty is calculated as the squared sum of the errors on the calculation of the TEDM from the measured Al, Si, Fe, Ca, K, and Ti elemental masses. By doing so, the percent uncertainty on the TDM is 12%.

2.4.2.2. Calculation of the mineralogical composition

The mass apportionment presented in Equation 1 has been performed as follows:

(1) the masses of quartz, calcite, dolomite, gypsum and feldspar (m_{quartz}, $m_{Ca\text{-}rich}$, $m_{feldspars}$) are quantified by XRD using the mass/intensity calibration curves as described in section 2.3.

(2) The mass of iron oxides ($m_{iron\ oxides}$) is measured directly by CBD analysis. The apportionment of $m_{iron\ oxides}$ into its main components (hematite and goethite) is performed by XANES spectroscopy.

(3) the mass of the clay species, kaolinite, illite, smectite, chlorite (m_{clays}) is estimated by the difference between the TDM and sum of the masses of m_{quartz}, $m_{Ca\text{-}rich}$, $m_{feldspars}$ and $m_{iron\ oxides}$. The apportionment of m_{clays} into its constituting species is difficult to achieve without a direct calibration. This is highly uncertain as there is basically no mineralogical reference having the same crystallographic and chemical status than in the actual aerosol samples, because of the exposure to the environment, weathering in particular, that they experience before and after become airborne. Furthermore, smectite clays are actually a family of species with different chemical characteristics (see the general chemical formulae in Appendix 1 for montmorillonite and nontronite). When only illite and kaolinite are present in the samples, and no traces of chlorite or smectite are shown by XRD analysis, their mass can be apportioned readily using the illite-to-kaolinite ratios (I/K) established by Caquineau et al. (2002) as a function of dust source region as

$$m_{kaolinite} = \frac{m_{clays}}{1 + \frac{I}{K}}$$
$$m_{illite} = m_{clays} - m_{kaolinite} \quad (2)$$

When smectites or chlorite is also detected, Equation (2) does not hold true. We will evaluate in the following sections the uncertainties induced by this approximation.

(4) The mass of titanium oxides $m_{tit\ oxides}$ is estimated by calculating the TiO_2 contribution as the measured elemental Ti multiplied by 1.67, the ratio between the atomic weight of TiO_2 and that of elemental Ti;

(5) The mass of organic compounds ($m_{organic}$) in mineral dust was generally neglected on the basis of the work by Lepple and Brine (1976), it should not exceed 3% of the TDM.

(6) We also did not take into account the mass of diatomite fragments which have been observed in samples originated from Bodélé (Chou et al., 2008). Diatomite fragments are silicate skeletons of algae and they do not have a crystalline structure which can be quantified by XRD analysis. Their presence can be put into evidence by elemental analysis as excessive values of the Si-to-Al ratio, up to 4 (Formenti et al., 2011b). The

diatomite mass can therefore be estimated by comparing the excess-SiO_2 mass calculated from elemental Si concentrations with respect to the mean ratio-to-Al to the mass of quartz estimated by XRD analysis. When doing so, the excess-SiO_2 mass is comparable to that of quartz except for the few samples for which dust originated from the Bodélé depression in which case their contribution to the TDGM is in the range 6–13%. This contribution is accounted in the error bars of the clay fraction for these samples.

3. Results

The whole dataset (ground-based and airborne AMMA SOP0 and AMMA SOP1-2, GERBILS and DODO campaigns) consists in 704 samples for which we measured the total elemental composition. Out of those, 54 samples have been selected to yield data on the major mineral composition, 86 have been analyzed to yield the content of iron oxide, 12 to determine the iron oxide speciation. 31 samples combined sufficient information to determine the full mineralogical composition. The sample selection has been based on the filter loading and on the possibility of identifying their provenance and attributing them a source region.

3.1. Identification of source regions

The identification of the origin of the mineral dust collected on the samples implies being able to make the link between the knowledge on the position and the mineralogy of the source regions to that of the aerosol samples. To do so, one should know (1) the transfer function, at emission, linking the soil mineralogical/chemical composition to that of the aerosols, and (2) the transfer function describing how its composition is modified during transport.

The first transfer function describes the mineralogical fractionation that occurs between the soil and the aerosol as a consequence of the size segregation happening when the soil grains blast on the soil after saltation (Rahn, 1976). The fractionation can alter the elemental ratio between Si and Al, as a result of the depletion in quartz and feldspars with respect to clays at emission. Quartz and feldspars have higher Si content than clays and are more abundant in the sand than in the silt/clay fractions of the soil (Mason, 1966; Rahn, 1976; Chatenet et al., 1996). These last are enhanced during emission by the saltation/sandblasting (Alfaro et al., 1998). Whereas there is still no systematic assessment of the transfer function between the soil and the aerosol composition, Claquin et al. (1999) have shown that some mass ratios between minerals (for examples, that of illite to kaolinite and that of calcite to quartz) are conserved from the soil to the aerosol if the comparison is restricted to roughly the same size fractions (clays or silt). Lafon et al. (2006) also suggested that the free-iron fraction to the total is conserved. Jeong (2008) has shown that the calcite and the K-feldspar fractions are very similar in Asian dust and the corresponding silty soil

fraction. The percent of phyllosilicate is higher in the dust aerosols than in the soil, whereas the quartz and plagioclase fractions are lower.

The second transfer function describes how the dust composition is modified during transport. Our dataset consists in data which have been collected at most 2 days after emission. We expect that only losses of particles of diameter larger than 10 μm would occur in this short time scale (Pye, 1987). We therefore assume that the chemical/mineralogical composition of our dust aerosol samples is linkable to that of the parent source regions.

To identify the pathway of air masses during transport, and trace them back to an active dust source, we used back-trajectory and dispersion modelling and various satellite products (e.g., Chou et al., 2008; Klaver et al., 2011). This approach does not apply to samples collected in the boundary layer during the Monsoon season south of the Inter-Tropical Convergence Zone (ITCZ). In this case, the dominant flow is from the south-west: dust is present in the boundary layer only as a result of erosion by organized convection or under particularly stable conditions, when high temperatures establish and the thermal turbulence in the boundary layer raises its top height at or above the shear level, bringing dust from the free troposphere in the surface level (Flamant et al., 2009; Formenti et al., 2011b).

Even when applicable, this approach has various caveats: first, if their horizontal velocity is high and exceed the local threshold velocity, air masses within the boundary layer might get loaded with dust along their way before reaching the sampling point. This happens for example when emission is induced by large scale frontal systems as the one of 3–7 March 2006 (Tulet et al., 2008). Secondly, ground-based sampling lasts several hours and the direction of air masses might change in between. Finally, aircraft samples integrate over large areas to which different air masses from different source regions might contribute. This problem might be overcome, or at least minimized, by increasing as much as possible the sampling frequency to match the variability of transport. We did that by following the variability of concentrations, in time or space, with ancillary measurements at higher temporal resolution (mass concentration by the TEOM balance, or the scattering coefficient by a TSI nephelometer).

In spite of this, we cannot exclude that our samples might represent larger emission areas than single "hot spots" (see for example, Figure 1 in Klaver et al. (2011)). We do not necessary regard this as a problem, as the atmospheric dust load, both at short and large-scale transport, is often due to a variety of sources active at the same time (Glaccum and Prospero, 1980; Reid et al., 2003; Formenti et al., 2003; Schepanski et al., 2007; Laurent et al., 2008; McConnell et al., 2008; Marticorena et al., 2010). Also, this supra-imposition, both in the vertical and in the horizontal, is what is actually seen by spaceborne sensors. The

482 results of this paper might then be used to build a dust composition model on a scale
483 relevant to satellites.

484 When doing so, we found that samples presented in this paper are representative of major
485 African sources which, according to Formenti et al. (2011) and Scheuvens et al. (2013), are
486 indicated as PSA (Potential Source Area) in Figure 2.

487 • The PSA2, including arid areas in Western Sahara, Mauritania and Morocco,
488 sampled during the DODO and the GERBILS campaigns. With respect to the extent
489 of this source, the northern part is under-represented as it was sampled on one
490 occasion only;

491 • The PSA3 represents emitting area in northern Mali and southern Algeria. This is
492 largely the dominant source in terms of frequency of sampling. The air masses
493 travelling from PSA3 often show a recirculating pathway over North Niger. By doing
494 so, at times they might pick up dust from the desert areas close to the Aïr massif,
495 which is not depicted in Figure 2, before reaching the sampling site. These
496 occurrences, when identified, are labelled as PSA3-NN;

497 • The PSA4 was sampled on a few occasions during wintertime. The PSA4 was
498 sampled on a few occasions during wintertime. As for PSA3, samples originating from
499 PSA4 for which the air masses had got in contact with the surface in northern Niger
500 when satellite images indicated emissions, have been labelled as PSA4-NN;

501 • A few samples also represent dust originated from the Bodélé depression (PSA5). In
502 summertime, a mixture of Sudan and Chad sources including Bodélé might have
503 been sampled (Flamant et al., 2009). Finally, a number of episodes of erosive
504 emissions by convection in the Sahel were also sampled and characterised
505 (referenced as Sahel). These occurred both over Mali and over Niger.

506 The PSA1 source is not represented in this paper as it was not sampled during the field
507 campaigns.

508

509 To provide with a first link between geographical origin and chemical composition, we traced
510 the scatterplot of elemental Si/Al versus Fe/Ca which we color-coded according to the source
511 region according to satellite/back-trajectories/dispersion modelling information. These ratios
512 have been shown previously to be rather robust indicators of the origin of mineral dust at the
513 large scale (Formenti et al., 2011a and references therein). The result is shown in Figure 3.

514 There are some clear distinctions which that can be made. Data points having Si/Al > 3 are
515 unambiguously identified as samples from the Bodélé depression, i.e. PSA 5. Their Fe/Ca

ratio is about 1. Data point having Fe/Ca > 3 are related to emission from erosive events in the Sahel. There are various sub-ranges in this group: data having Fe/Ca in the range 3–5 correspond to transported dust aerosol from the Sahel, sampled 1–2 days after emission, corresponding to mixed sources, as PSA3 + Sahel. Data having Fe/Ca > 5 correspond to samples collected immediately or at the very early stage after emission by convective events, mostly locally at the ground-based Banizoumbou site (when the Fe/Ca ratio exceeds 10), but occasionally on uplifted dust onboard aircraft.

Data with Si/Al in the range 2.5–2.9 and Fe/Ca in the range 1–3 have their origins mostly at latitudes in the range 16–27°N, i.e. PSA 3. Whereas the variability of the Si/Al ratio is low, that of Fe and Ca can be used to make some distinctions amongst sources. Fe/Ca higher than 1 is measured for data points from northern Mali, Mauritania, Algeria, northern Niger and Libya whereas Fe/Ca < 1 is for dust from Western Sahara (PSA 2). For this source, there are two clear outliers corresponding to samples of dust originating from Morocco and showing the lowest Fe/Ca ratio (~ 0.4).

3.2. Mineralogical composition

The investigation of the mineral composition is based on 51 samples, 15 of which collected onboard aircraft. This dataset represents a diversity of sources and emission conditions.

The most evident peaks, for all samples, are those of illite, kaolinite and quartz. Less evident, and not ubiquitous, are the peaks corresponding to feldspars (albite and ortoclase), and calcium-rich minerals (calcite, dolomite, gypsum). Feldspars are found in the samples from local erosion and South Algeria/North Niger/Mauritania and Western Sahara. This last set might also contain calcium-rich minerals. Smectite clays are detected as a large and rather weak peak at angles comprised between 4 and 7°. This is indicative of the fact that smectites are a family of weathered clays of different chemical composition (e.g., montmorillonite, nontronite), whose crystalline structure can be heavily modified in the environment. Smectite clays were only evident in samples originated from South Algeria/North Niger/Mauritania and Western Sahara.

We can obtain the mass fractions of minerals which can be detected by X-ray diffraction by using the calibration factors as described in section 2.3.2 (Figure 4).

Regardless of the origin, clays and quartz account in average for 87% (± 6) and 10% (± 6) of the diffracting mass. There is only one clear outlier in an episode of intense local erosion sampled at the Banizoumbou super-site (sample SOP1-8), for which the percent clay fraction is reduced (56%), and the quartz and feldspars fraction enhanced (41% and 3.3%, respectively). This is consistent with the fact that at erosion the size distribution shows an

550 enrichment of coarse particles, whose composition should be closer to that of the soil silt
551 fraction (Gillette and Walker, 1977; Chatenet et al., 1996).

552 The analysis of the XRD spectra also show that kaolinite and illite are very often the only clay
553 species detected. A broad peak corresponding to smectites was detected on samples from
554 Algeria and at times Bodélé, consistently with finding of Moreno et al. (2006). No chlorite has
555 been detected in our samples. As explained in section 2.4.2.2, the relative proportions (by
556 mass) of illite and kaolinite have been estimated using the origin-dependent ratios
557 established by Caquineau et al. (2002). For the sources considered in this dataset, the illite-
558 to-kaolinite ratios could vary between 0.1 and 2.3. The central and western Saharan sources
559 (PSA2 and PSA3) display the highest values (1.6 to 2.3) for PSA 5, Northern Niger and
560 Sahel the lowest values (0.1 to 0.7).

561 ## 3.3. Iron oxides content and speciation

562 The quantification of the content of iron in the oxide form (Fe_{ox}), that is free iron which is not
563 in the crystal lattice of alumino-silicates, has been performed on 81 samples of different
564 origins and load (33 out of those have been collected onboard aircraft). In average, Fe_{ox}
565 account for 58 ± 7% of the mass of elemental Fe. The range of variability is illustrated in
566 Figure 5.

567 The lowest values (down to 44%) are found for samples of dust originating from the PSA4
568 (Chad/Egypt) area and for a set of samples collected above the PSA2 areas. The highest
569 values (up to 71%) are obtained for samples of dust emitted by local erosion in the Sahel,
570 including one episode in which uplifted dust has collected onboard aircraft after emission.
571 Other subsets of samples, such as those of dust originated from the South Algeria/North of
572 Niger areas, display equivalently high values when during long-range transport, dust from
573 Algeria mixes with locally-produced dust in Niger. It should be noted also that, because of the
574 internal variability of each group, there is no statistically-significant difference between the
575 iron oxide fractions of the total iron for long-range transported dust originated at latitudes
576 north of 16°N. A broad distinction between the Fe_{ox}-to-Fe ratio of Sahelian samples with
577 respect to those of Saharan samples can be made by sorting the data points by their
578 corresponding Fe/Ca ratio. Mineral dust emitted from the Sahel (Fe/Ca > 3) are
579 characterized by a mean Fe_{ox}-to-Fe ratio value of 65% (± 5%, standard deviation of the
580 mean), whereas episodes of transport from the Sahara (Fe/Ca < 3) are characterized by a
581 mean ratio of 56% (± 6%). No further distinction based on origin is possible in this second
582 group of samples. This is illustrated in Figure 6.

583 X-ray absorption spectroscopy on twelve samples of differing origins indicated that goethite
584 is overall the dominant species of iron oxides. Goethite accounts for 48 to 73% of the iron

585 oxide mass, whereas hematite accounts for 27 to 52%. These values do not show a clear
586 trend with respect to the sample origin. The relative proportions of iron in the form of
587 hematite and goethite with respect to total iron are shown in Table 2.

588 ## 3.4. Titanium oxides content

589 Titanium oxides deserve attention as they are involved in photo-catalytical heterogeneous
590 reactions with various atmospheric constituents, including volatile and semi-volatile organic
591 compounds which are found in transport regions of mineral dust due to biomass burning
592 emissions (Gustafsson et al., 2006).

593 We therefore examined our dataset in order to provide with estimates of the content of
594 titanium oxides in mineral dust from various sources in western Africa. The titanium oxide
595 content has been estimated from the measured element Ti concentration (obtained by XRF)
596 which is converted to TiO_2 using the appropriate molar mass conversion factor (1.67). This
597 should be considered as an upper limit estimate as some of the titanium in mineral dust is
598 present as substitution element in aluminosilicates (Dolcater et al., 1970).

599 Figure 7 presents the correlation between the TiO_2 and the TDM. Two populations can be
600 identified: one corresponding to samples collected in correspondence of erosion events and
601 one corresponding to advection events. For both populations, the correlation is excellent (R^2
602 equal to 0.97 and 0.92, respectively) and the scatter of points is minimal. The TiO_2 content is
603 higher in erosion events from the Sahelian region (average 1.2% (± 0.1) of the mass), than
604 for advection events of Saharan dust, for which TiO_2 represents in average 0.71% (± 0.01) of
605 the mass.

606 Looking at the elemental ratios between Ti, Fe, and Fe_{ox} provides with further insights
607 (Figure 8). The ratio of Ti-to-Fe is insensitive to changes in the Fe_{ox} proportions to Fe up to
608 60%, and then starts increasing linearly with increasing Fe_{ox}-to-Fe ratio. This suggests that,
609 in Sahelian dust, Ti is associated with iron oxides but not in Saharan dust.

610 ## 3.5. Mass apportionment of the mineralogical composition

611 By combining the information presented in section 3.1 to 3.4, we can estimate the
612 mineralogical composition of samples of mineral dust of local or distant origin.

613 The mass apportionment is shown in Table 3. Note that we provide here with the
614 composition of the bulk mineral dust, without explicitly taking into account the dependence on
615 size.

616 There are clear similarities in the composition of the dust from those different origins, first of
617 all in the fact that the clay fraction represents the largest fraction of the dust mass. Also note

618 the absence of Ca-rich minerals (calcite, dolomite, gypsum) in dust originating from the Sahel
619 compared to that originated elsewhere.

620 Despite the overall similarities, there is indeed a large internal variability within each source
621 group, expressed by the standard deviation around the mean, and which might be related to
622 either the time or height after transport.

623 An example can be given by looking at the composition of the four samples in Bodélé/Sudan
624 group: one sample was collected in the dry season, whereas the remaining three are
625 sequenced samples collected in the wet season, at a time characterised by the absence of
626 local emission, but by a progressively increasing entrainment of dust transported from the
627 free troposphere to the surface layer (J. L. Rajot, pers. comm.). These wet-season samples
628 have a lower clay fraction and a higher quartz and feldspar content (in the range 7–18% and
629 0.4–0.8, respectively). This variability corresponds to differences in the volume size
630 distribution, normalised to the total volume for sake of comparison (Figure 9). As a matter of
631 fact, the volume size distribution of the dry-season sample presents a large coarse mode
632 peaking around 4–5 μm, whereas the wet-season samples have a bimodal volume size
633 distribution with an additional mode centred at 8 μm. Within this group, the sample having the
634 largest quartz fraction is also the one displaying the larger fraction of particles above 10 μm.

635 A second example of the links between time after emission, size distribution and
636 composition, is given in Figure 10 showing the normalised particle size distributions (by
637 volume) for one case of Sahelian dust by local erosion (sample SOP1-8), two samples
638 representing the background dust composition in the absence of local erosion (SOP1-15 and
639 SOP1-60) and one case representing the composition of Sahelian dust advected at the
640 sampling site after having been emitted by local erosion in the proximity (SOP1-17). There
641 are clear differences between these cases: sample SOP1-8 has a mode at 8 μm and the
642 largest coarse particle fraction. Samples SOP1-15 and SOP1-60 have a bimodal size
643 distribution with modal diameters at 3–4 and 8 μm. Finally, only the mode 3–4 μm remains
644 for sample SOP1-17. As for the case presented in Figure 9, it is evident from Figure 10 that
645 the coarse mode at 8 μm bears the most of the quartz and feldspar mass fractions, and that
646 the dynamic evolution of this mode controls the content of quartz and feldspar in dust. The
647 comparison of Figures 9 and 10 also suggests that, once the mode at 8 μm is deposited,
648 differences in the mineralogical composition of mineral dust will be more independent of the
649 size dynamics and reflect better differences in the mineralogy of the parent soil.

4. Discussion

4.1. Comparison with other datasets

All comprehensive papers relating on the composition of mineral dust state that the comparison of compositional data from different datasets depends critically on the experimental conditions, in particular the duration and location of sampling (integration time, near-source location) (Formenti et al., 2011a; Scheuvens et al., 2013). These considerations are particular relevant to aircraft sampling where the difficulty in controlling the size cut-off of samplers generally disfavour the coarse particle fraction in an often non-quantified way (Formenti et al., 2011a). Furthermore, as the aircraft is moving during sampling, a 20-minute aircraft sample will represent a distance of the order of 120 km, which might integrate the contribution of various sources (Klaver et al., 2011).

As a consequence, the integration and the comparison of different datasets of the composition of mineral dust is not a straightforward exercise.

Overall, our results indicate the dominance of clays in the dust composition when only the aerosol fraction is measured. In this respect, they are in accordance with previously published papers for dust collected in Africa (Kandler et al., 2009) or after long range transport (Delany et al. 1967; Kiefert et al., 1996; Glaccum and Prospero, 1980; Caquineau et al., 2002). These measurements, however, tend to indicate that the clays fraction accounts for ~60-70% of the dust weight, whereas our measurements suggest higher values (80-90%). It should be reminded that the determination of the mineralogical composition will depend on the crystallography of the standard minerals used for calibration, and on the normalisation to the total dust mass. In our work the percentage of clays in dust depends directly on the normalisation factor, on which we have an uncertainty of the order of 17%, as we do estimate clays from the difference between the total dust mass and the calibrated mass of non-clay compounds. As an example, Glaccum and Prospero (1980), using standard clays minerals for calibration, estimate that the crystalline mass represented 70 to 110% of the weighed mass. These values reflect, at least partially, the uncertainty on the clay fraction.

Nonetheless, in some cases differences might be due to sampled aerosol size distribution. As a matter of fact, the lowest detected percentage of clays corresponds to sample SOP1-8, collected during an intense episode of local erosion. In this case, clays account for around 50% of the measured mass, in accordance with measurements by Caquineau et al. (1997; 2002) in similar conditions.

This is also clear for example by looking at the data published by Kandler et al. (2009), who documented the dust composition in dust storm (total suspended particulate concentrations higher than 300,000 μg m^{-3}) and low dust periods (total suspended particulate

concentrations around 100 μg m^{-3}) in Morocco. Quartz accounts for as high as ~65% in dust storm conditions, suggesting that soil grains, and not only aerosols, were sampled. Conversely, low-dust conditions are characterised by only about 20% of quartz. These authors showed that, for locally emitted dust, illite is the dominant clay form over kaolinite (up to 30 and 5% by volume, respectively). These authors also detected clay in the form of chlorite (less than 10% by weight) and calcite (up to 15%).

Few authors have published data on the iron oxide content. Lafon et al. (2004) evaluated the free-to-total iron content in samples collected at the Banizoumbou ground-based site and found mean values of 0.44 (± 0.11) and 0.65 (± 0.04) for dust transported in the Harmattan flow (from the Sahara) and dust emitted locally by convective erosion. Lazaro et al. (2008) found sensibly lower values than ours ranging from 0.26 to 0.63 but only exceeding 0.56 in three occasions when back-trajectories indicated transport from the Sahel or a mixture of dust originating from the Sahara and the Sahel. Our values are on the higher side with respect to those of these authors. Nonetheless, the back-trajectories presented in the paper seem indicating that the Saharan dust originated from higher latitudes that the one we sampled – and mostly from Tunisia and Algeria. It will be interesting in the future to sample those source areas to confirm these rather low values.

Finally, our results on the iron oxide speciation are consistent with findings of different authors using XANES speciation (Wilke et al. 2001; Ohta et al., 2006; Prietzel et al. 2007; Majestic et al., 2007) and visible spectroscopy (Arimoto et al., 2002) indicating that Fe(III) is the dominant red-ox form of iron oxides and that goethite is the predominant form of iron oxide over hematite.

4.2. Atmospheric implications

The results showed in this paper suggest that, when restricted to the mass fraction below 20 μm, the dust composition in western Africa may apparently be simplified to few minerals, clays, quartz, calcite, iron and titanium oxides. Feldspars and other calcium-containing minerals such as dolomite and gypsum are very minor components close to detection limits. The geographical distribution of the dust composition is relatively unimportant in terms of mass fractions, in particular in comparison to the importance of the size distribution whose variability with time seems to be able to explain some differences observed between samples from the same source region at different times after emission. Nonetheless, it is important to evaluate whether differences in the composition at the regional scale, even when minor, might give raise to differences in the impacts of mineral dust.

To do so, we explore the influence of dust composition on the spectral complex refractive index $\tilde{n}$ and the fraction iron solubility.

720 **4.2.1. Implications for optical properties**

721 As a mean of evaluating the effect of the variability of the composition on the dust optical
722 properties, the volume-average refractive index has been calculated as

723

724 $$\tilde{n} = \sum_j f_j \times \tilde{n}_j \quad (4)$$

725

726 where f_j is the volume fraction of each individual mineral in the dust sample (as reported in
727 Table 3) and $\tilde{n}_i$ is its complex refractive index. Equation 4 assumes that minerals in dust are
728 in internal mixing. In reality, minerals are present in dust as external mixtures, with the
729 exception of iron oxides which may be found as inclusions in clays (Sokolik and Toon, 1999).
730 However, the internal mixing hypothesis is frequently used in experiments and climate
731 models (e.g., Balkanski et al., 2007; Kandler et al., 2009; McConnell et al., 2010; Hansell et
732 al., 2011),

733 Values of the complex refractive index $\tilde{n}_j$ of the individual minerals detected in our samples
734 are listed in Table 4. We have restricted the calculations to two spectral domains: the near
735 UV-visible between 370 and 700 nm and the thermal IR from 8 to 15 µm, where values for all
736 individual minerals are available.

737 Results are presented in Figure 11, where they are compared to the values of the "desert"
738 dust aerosol model in the OPAC (Optical Properties of Aerosols and Clouds) database (Hess
739 et al., 1998), often used in satellite retrieval algorithms in the thermal infrared (see Table 1 in
740 Klüser et al., 2012), but also in radiative transfer calculations (Highwood et al., 2003;
741 Haywood et al., 2005). The "desert" model in the OPAC database represents the properties
742 of mineral dust at source region, considered as a mixture of quartz and clays in different size
743 fractions.

744 We restrict Figure 11 to the visible and infrared imaginary parts of the complex refractive
745 index $\tilde{n}_i$,. In the visible, the imaginary part of the complex refractive index is relatively
746 constant with wavelength. Mean values are of the order of 0.003, with standard deviation of
747 the order of 0.001, with the exception of data from the PSA4 source, which average at 0.006
748 and present a standard deviation (0.003). It is difficult to judge on this variability as it is
749 induced by one sample only presenting an outstanding iron oxide fraction. In the infrared, the
750 imaginary part shows a band-type structure in correspondence to the major absorption bands
751 of clays and quartz, mostly found in the atmospheric window between 8 and 11 µm. There is
752 very little sample-to-sample variability in the position of the bands, as well as in the relative
753 proportions of the band peaks, with the exception of the Sahelian dust samples, which

754 present a larger standard deviation due to the enhancement of the band at 9.2 μm
755 corresponding to the outstanding quartz fraction of sample SOP1-8. There is very little
756 difference in the spectra of sources PSA3, PSA4 and to a lesser extent PSA5, which have
757 the highest absorption values at 9.6 μm. However, the spectral dependence for dust from
758 source PSA2 is different (peak at 9.2 μm more pronounced than that at 9.6 μm).

759 The composition-based refractive indices calculated in this work are very different to those of
760 the OPAC database. Below 0.6 μm, the volume-averaged values are on the lower side than
761 the OPAC values, with the exception of values for the PSA4 samples, due to their larger
762 standard deviation. Above, the two datasets approach. The spectral dependence is also
763 inconsistent, and reflects the reduced spectral variability of the values for iron oxides (both
764 hematite and goethite) in Bédidi and Cervelle (1993) with respect to other commonly used
765 databases, such as that of Shettle (1979) for hematite on which OPAC is based.

766 The calculated volume-average infrared values in the absorption band between 8 and 10 μm
767 are two times higher than in the OPAC database. The main reason for that is the volume-
768 mixing rule which enhances absorption. Additionall, for single-mineral species, various
769 authors (Hudson et al. 2008a, 2008b; Mogili et al., 2007, 2008) found strong differences in
770 peak positions and spectral shape between extinction spectra measured by Fourier-
771 transform infrared spectrometry and those calculated from published optical constants. All
772 these studies show residual differences suggesting that optical constants might vary
773 depending on whether they had been determined on powders or bulk samples, on the
774 degree of water association of minerals, and on their chemical form (substitutions,
775 impurities). As this variability might be even larger when looking at actual dust samples, the
776 comparison clearly suggests that new measurements of IR extinction spectra on real dust
777 samples representative of the mineralogical composition of the different source areas are
778 required.

779 **4.2.2. Implications for Fe fractional solubility**

780 The solubility of dust iron is a function of iron speciation, i.e. oxidation states, bonding
781 environments and mineralogy (Journet et al., 2008; Schroth et al., 2009). Thus, due to higher
782 solubility of iron trapped in the crystal lattice of aluminosilicates and the large abundance of
783 clay minerals, Journet et al. (2008) suggested that the use of hematite as a single source of
784 *DFe* in biogeochemical models might cause an underestimation of the *DFe* supply to the
785 ocean. On this assumption, Paris et al. (2011) showed that the iron fractional solubility from
786 analogue of mineral dust can be estimated as the sum of Fe solubility of various minerals
787 compounding iron in the dust matrix. We propose to apply this calculation to this dataset to
788 estimate the solubility of dust in source region. For this purpose, we use the iron solubility

789 from minerals measured by Paris et al. (2011) at pH = 4.7 which a typical pH of African
790 rainwaters (Desboeufs et al., 2010), i.e. *SFe* equal to 0.17% for illite and 0.006% for free iron
791 from goethite and hematite. Paris et al. (2011) made the approximation that all the iron
792 associated to clay is present as illite. Journet et al. (2008) emphasized that even the iron in
793 impurities into kaolinite or feldspars matrix present a high solubility. Our measurements show
794 the predominance of kaolinite in comparison to illite, so we consider also the dissolution of
795 Fe from kaolinite due to the large proportion of this mineral in the studied samples. We use a
796 *SFe* = 0.63% for kaolinite (Paris, personal communication). The percent quantity of feldspar
797 being usually inferior to 1% in the samples, we neglect the iron associated to these minerals.
798 Smectites, such as montmorillonite, are also minerals with high content of iron with a higher
799 solubility (Journet et al., 2008). However, due to the difficulties in quantifying the smectite
800 fraction, this other source of structural Fe is not well constrained. Moreover, Shi et al. (2011)
801 mention the presence of highly-soluble nanoparticles of ferrihydrite or poorly crystallized iron
802 in fine fraction of soils. However, the quantification of this iron phase is obtained by
803 sequential extraction and is difficult to apply on field samples due to the low mass. So we are
804 not able to consider this species in our calculation.

805 Among the samples present in our database, the mineralogical composition including
806 goethite, hematite, illite and kaolinite is evaluated for 27 samples, enabling to calculate the
807 iron fractional solubility (Table 3). In this case, the iron content in illite is assumed equal to
808 4.0 ± 0.9%, which corresponds to the mean stoichiometric value of two types of illites
809 (Fithian, Illinois and Rochester, Minnesota, as shown in Journet et al., 2008). The iron
810 content in illite can vary from 0.8% to 8.4 % (Murad and Wagner, 1994), this large range is
811 due to the fact that Fe is present as substitution of Al or K in the sheet-like structure of illite,
812 and this will depend on the environmental conditions that the clay has experienced in the soil
813 fraction (weathering,...). In goethite and hematite, we estimated the iron content based on the
814 analysis of Journet et al. (2008) and Paris et al., (2011) as 62.9% and 57.5% for goethite and
815 hematite, respectively. For kaolinite, Mestdagh et al. (1980) show that the iron content is
816 related to the cristallinity of the mineral and ranges from 0.02% to 0.81% with an average of
817 0.4% ± 0.2%, which is used for our calculation.

818 In order to have a larger view of the variability of iron solubility as a function of emission
819 source, we can also calculate iron solubility from the partitioning between structural and free
820 iron as obtained by the CBD extraction analysis (Table 2). This is doable for 85 samples,
821 among which the 27 samples for what the mineralogical composition is estimated. In this
822 case, we consider the stuctural iron ($\%Fe_{structural}$) is associated to illite ($\%Fe_{illite}$) and kaolinite
823 ($\%Fe_{kaolinite}$) in the proportion of illite-to-kaolinite ratio corresponding to the origin of the
824 samples (see 3.2), such as:

$$\%Fe_{kaolinite} = \frac{\%Fe_{strutural}}{\left(1 + 10 \times \frac{I}{K}\right)}$$

and $$\%Fe_{illite} = \%Fe_{structural} - \%Fe_{kaolinite}$$

with 10 represents the illite-to-kaolinite iron content ratio (4.0%/0.4%)

Results are summarized in Figure 12.

The mean value of iron fractional solubility is 0.10% (± 0.02%) whatever the methods of calculation, i.e. from mineralogical composition or from CBD extraction analysis. There is little variability of iron solubility as a function of the source; nonetheless, this is directly opposite to the iron oxide content, i.e., the lowest values (0.08% ± 0.01%) obtained for samples of dust emitted by local erosion in the Sahel, in agreement with the highest iron oxides content. Inversely, the samples with the highest solubility (0.13% ± 0.01%) issued from PSA3, i.e. South Algeria/Mali which present a low % of free iron (49%). Data show that 54 to 87% of soluble iron is structural iron associated to illite, meaning that this mineral is the major provider of soluble iron in our conditions of calculation. The determining factor for this parameter is the quantification of illite and hence the hypothesis made on the illite-to-kaolinite ratio as a function of emission source, which is estimated from Caquineau et al. (2002). Thus, the regional variability on iron solubility obtained here is mainly associated with this ratio which should be better constrained. A rapid calculation for the PSA3 samples, the richest in structural iron, show that the iron solubility is divided by a factor 2 when I/K varies from 0.1 to 2.3, the extreme values observed by Caquineau et al. (2002). This means that the solubility between the various emission sources varies at the best by a factor 2. Another source of error could be the estimation of iron oxide which is affected by 30% errors (and those of illite too, by extension). Sample-to-sample comparison shows that there is a rather good correspondence with the two methods of calculation (within 15%). However, the calculation based on mineralogy yields values lower by a factor of 1.5 for the samples issued from PSA3 alone or in mixing with other sources, meaning an underestimation of structural iron in comparison from the direct measurements by CBD analyses. Smectites are identified for several samples of this source, we underestimate so the calculated solubility for the samples where these minerals are present.

The mean fractional iron solubility obtained by calculation is consistent but rather inferior to the observations obtained for transported Saharan dust over Atlantic which ranges from 0.12 to 4.1% (Sarthou et al., 2003; Baker et al., 2006; Sholkovitz et al., 2012). However, our calculation are exclusively based on mineralogical parameters, since our samples have been

collected at most 2 days after emission and do not integrate the various chemical and physical processes increasing dust solubility during long range transport, as cloud process (Desboeufs et al., 2001); photochemical process (Hand et al., 2004) or organic complexation (Paris et al., 2013). Thus, the range of calculated values could be representative of iron solubility for the various sources of African dust before transport. Moreover, the limited regional variability estimated here in comparison to the variability of measurements over Atlantic Ocean show that the emission source of dust is less critical than the process after transport to estimate the fractional iron solubility of dust. Nevertheless, new direct measurements of the iron fractional solubility for sources of dust in Western Africa are necessary to validate these conclusions.

5. Final remarks, conclusions and perspectives

In this paper we have presented an insight on the mineralogical composition of mineral dust from Western Africa from the synthesis of the airborne and ground-based observations of field campaigns conducted between 2006 and 2007. These observations have been performed at emission or within 2 days of transport in the atmosphere. The strength of this synthesis resides in the fact that the observations have been performed in a consistent way from the methodological point of view (both for the sample collection and analysis) and that they span a large geographical region covering some of the major African dust sources.

The composition data presented in this paper are being made public on a dataset called DUST-MAP, to date still on its trial version. Meanwhile, data are available upon request. The perspective evolution of this dataset will be the inclusion of data from other field campaigns, both close to source regions and at some distance. Amongst those are the FENNEC and the SAMUM field campaigns (Heintzenberg et al., 2008; Ansmann et al., 2011; Washington et al., 2013), which were conducted downwind sources in Algeria and Morocco relevant to large-scale transport (Caquineau et al., 2002). This will require a close-up examination of experimental protocols and a careful evaluation of their influence on the results.

The presentation of this work deserves some final considerations and opens various perspectives.

The bulk mineralogical composition of dust in Western Africa can be described by a simple model where kaolinite and illite account for 80% or above of the mass, and quartz, iron and titanium oxides for the remaining 20%. Calcite is a distinctive element of Saharan sources for which it ranges between 0.3 and 8.4% in dust mass. For the remaining minerals, the variability is due to source type (e.g., the proportions of illite and kaolinite as evidenced by Caquineau et al. (2002)) or to differences in the size distribution, particularly the increase of the quartz fraction corresponding to a coarse mode centred around 8 μm in diameter. For the

first time to our best knowledge, we provide with a large dataset of titanium oxide data which can be relevant to atmospheric photochemistry (N'Dour et al., 2009). We estimate that Sahelian dust is composed by 2% (by mass) of titanium oxides, that is, double the mass fraction of dust from sources in the PSA2, PSA3, PSA4 and PSA5 areas, with very little sample-to-sample variability. Iron oxides, also important for atmospheric chemistry processes and radiation, display higher values in Sahelian than in Saharan dust.

The discussion of the regional variability of the mineralogical composition is based on our ability in detecting source areas based on satellite remote sensing or on soil properties map (e.g., Claquin et al., 1999; Schepanski et al., 2007; Laurent et al., 2008; Ginoux et al., 2012; Nickovic et al., 2013; Journet et al., 2014), and in attributing the provenience of an air mass to it via back-trajectory calculations (e.g., Klaver et al., 2011). Beside the uncertainties inherent to the detection of sources, there are two additional factors of ambiguity in source attribution: first, air masses, especially during winter-time, mostly travel in the boundary layer and might uplift dust aerosols at various times before reaching the sampling site; secondly, aircraft samples might integrate transport from various sources active at the same time due to the fact that aircraft moves during sampling and that sample collection lasts at least 20 minutes, which corresponds to about 120 km at typical aircraft cruise speed (see Figure 1 in Chou et al., 2008 and Figure 1 in Klaver et al., 2011). It is therefore clear that some fine features of the mineralogy specific to individual sources might be lost. Nevertheless, our data well represent the composition of the regional dust load as it results from the natural mixing occurring during transport. They are also of comparable spatial resolution to that of various state-of-the-arts global and regional circulation models including dust mineralogy (Balkanski et al., 2007; Hoose et al., 2008; Huneeus et al., 2010). Henceforth, the composition data presented in this paper may serve to evaluate the regional and global model estimates of the dust mineralogical composition in the Western African atmosphere and to calculate dust properties relevant to their direct, indirect and biogeochemical impacts. Claquin et al. (1999) have discussed some comparisons between the mineralogy of dust atmospheric data and that of the soil fraction predicted by a surface mineralogy table constructed from maps of the arid soil mineralogy (updates of this table have been recently published by Nickovic et al. (2012) and Journet et al. (2014)). To do so, these authors have calculated weight ratios between some minerals (calcite, feldspar and hematite, where hematite is meant to represent the sum of the content of goethite and hematite) with respect to quartz. Our data are consistent with the Claquin et al. (1999) dataset regarding the variability of the calcite-to-quartz ratio, but display higher and lower ratios for hematite and feldspar, respectively. Our ratio of hematite-to-quartz ranges between 0.03 and 1 (0.09 and 3 when the sum of goethite and hematite is considered) instead than 0.009–0.09, whereas our ratio feldspar-to-quartz is

928 in the range 0.03–0.11 instead that 0.2–2 in Claquin et al. (1999). These differences illustrate
929 the fact that our data are closer to representing the clay soil fraction, whereas the data of
930 Claquin et al. (1999) best represent also the silt fraction, richer in quartz particles. When
931 limited to sample SOP1-8, the local erosion sample enriched in quartz and in the particle
932 fraction larger than 20 μm, ratios are 0.09 for hematite-to-quartz (0.03 if hematite only is
933 considered) and 0.08 for feldspar-to-quartz, in the range expressed by Claquin et al. (1999).

934 Finally, we have provided with the estimate of parameters relevant to the direct impact of
935 mineral dust on radiation and on ocean productivity: the complex refractive index $\tilde{n}$ and the
936 iron fractional solubility *SFe*.

937 Assuming internal mixing, we have shown that the complex index of refraction based on
938 mineralogy has some variability mostly related to the partitioning between illite and kaolinite
939 and to the quartz fraction higher than 40% of the dust volume. The spectral behaviour of the
940 estimated complex index of refraction is quite different from the OPAC database. The OPAC
941 approach overestimates absorption in the visible. On the other hand, a very recent study
942 presents values of the complex refractive index in the shortwave based on a global
943 mineralogy soil map (Schmid et al., 2013). At 550 nm, these authors predict a real part of the
944 complex refractive index around 1.56, that is, higher than our which ranges between 1.45
945 and 1.51. Their imaginary part averaging at 6.2×10^{-4}, that is, almost an order of magnitude
946 lower than our predicted values (average 3×10^{-3}). This is the consequence of the fact that
947 optical properties estimated from the soil fraction will reflect more closely the optical
948 properties of quartz, which, is enriched in the soil fraction but which in the aerosol fraction
949 due to the size fractionation at emission. An additional confirmation is given by the fact that,
950 in our data, the highest value of the real part of the complex refractive index is obtained for
951 sample SOP1-8, representing the Sahelian erosion case with the highest quartz fraction
952 (41% by weight), whereas the highest values of the imaginary part are obtained for samples
953 representing long-range transport from Libya through north Niger, having a low or even the
954 lowest quartz percentage by weight (1.5–6%) but having the highest calcite fraction (4–8%
955 by weight). As a matter of fact, quartz is transparent in the visible, whereas calcite, but also
956 clays are absorbing. These considerations bring to the conclusion that not only the soil
957 mineralogy but also the transfer function between the soil and the aerosol fractions must be
958 implemented in models estimating the dust optical properties.

959 In the longwave spectrum, our calculations suggest higher absorption than the OPAC model
960 in the atmospheric window. The 10–12 μm band, which is sensitive to differences in the
961 mineralogical composition amongst sources, is relevant to the retrieval of various space-
962 borne sensors, including IASI, AIRS, and MODIS (De Souza Machado et al., 2006; Hudson
963 et al., 2008; Klüser et al., 2011; Laskina et al., 2012). Some of the discrepancies between

964 our values and the OPAC database to be, at least partially, due to differences in the optical
965 constants of the individual minerals. Dedicated in situ measurements of the optical constants
966 of the dust samples would allow confirming this hypothesis.

967 Nonetheless, a limitation of this work, impacting our estimate of the complex refractive index,
968 is the quantification of smectite-type clays. For the purposes of the present study, we have
969 chosen to neglect the contribution of smectites, which were detected only on a few samples,
970 and which we consider as a trace component of the aerosol. Also, smectites are dominant in
971 the 0.2 μm size fraction, which is poor in mineral dust in our samples (Klaver, 2012).

972 In the visible Egan and Hilgeman (1979) indicated that two different montmorillonite types
973 (one from Wyoming and one from Mississippi) have very similar refractive indices, to those of
974 either kaolinite or illite, both in spectral dependence and magnitude. However, below 500 nm
975 the imaginary part of the complex refractive index of the montmorillonite from Mississippi is
976 higher by a factor of 2 than that of illite, reaching 0.004 between 200 and 360 nm. In the
977 infrared, various authors (Toon et al., 1976; Glotch et al., 2007; Hudson et al., 2008) have
978 shown that montmorillonite has similar optical properties to those of illite, albeit displaying
979 higher intensity of extinction around 9.5 μm, in the Si–O stretching band. Köster et al. (1999)
980 examined 5 types of nontronites and Fe-rich smectites and found that the position and the
981 intensity of this band vary depending on tetrahedral Fe(III) content. Also, the speciation of
982 clays, in particular that of montmorillonite, has implications for the cloud and ice nucleation
983 properties of mineral dust and the estimate of iron fractional solubility (Hoose et al., 2008;
984 Journet et al., 2008). Ultimately, these facts depend on the compositional heterogeneity in Al-
985 rich smectite in the natural soils and sediments (Christidis and Dunham 1993, 1997;
986 Christidis, 2006), due to various processes, including weathering and/or hydrothermal
987 alteration of basic rocks (Köster et al. 1999), but also reduction reactions of structural Fe by
988 microorganisms (Pentrakova et al., 2013). This makes their quantification extremely
989 dependent on the environmental conditions. Similar considerations will held for chlorite-type
990 clays, which were not detected in our samples, but might be present in dust from North
991 African deserts such as Morocco and Tunisia (Paquet et al., 1984; Kandler et al., 2009). It
992 should be noted that to date no measurements of the complex refractive index of chlorites
993 are available in the shortwave. In the longwave, chlorite has significantly different optical
994 properties than illite and kaolinite, in particular concerning their major absorption bands,
995 which is located at 9.6 μm for illite and kaolinite, and at 10.2 μm for chlorite (Egan and
996 Hilgeman, 1979; Mooney and Knacke, 1985). Should chlorite be detected in the samples, its
997 lack of quantification will be treated as an additional source of error to be evaluated.

998 Regarding the iron fractional solubility, our data are not conclusive in identifying a clear
999 regional difference with respect to the variability observed for dust collected over the Atlantic

Ocean after short- and long-range transport. This limited regional variability suggests that a single reference value (0.1%) of the fractional solubility *SFe* of Saharan and Sahelian dust before atmospheric transport could be used in biogeochemical models. Direct field measurements of *SFe* close to emission sources, unavailable at the moment, are needed to confirm this finding. Finally, the *SFe* value estimated for dust near source regions is in the lowest range than values obtained for dust collected over the Atlantic Ocean, pointing to the need of taking atmospheric processing into account when iron solubility is ought to be described at the global scale.

Acknowledgements

This research was funded by several institutions. Based on a French initiative, AMMA was built by an international scientific group and is currently funded by a large number of agencies, especially from France, the United Kingdom, the United States, and Africa. It has been the beneficiary of a major financial contribution from the European Community's Sixth Framework Research Programme. Detailed information on scientific coordination and funding is available on the AMMA International Web site at www.amma-international.org. Financial support by the API-AMMA and LEFE (project BIRD) French national funding programs is also acknowledged. The participation of P. Formenti to the DODO and GERBILS field campaigns was supported and by the UK NERC and by the UK MetOffice, which are gratefully acknowledged.

Thanks are also due to the LISA personnel who participated in field campaigns and helped with sample collection, as well as to the BAe-146 and SAFIRE air and ground crews, as well as the FAAM and Met Office observers.

References

Abdourhamane Toure, A., Rajot J.L., Garba, Z., Marticorena, B., Petit, C., Sebag, D. 2011 Impact of very low crop residues cover on wind erosion in the Sahel. Catena, 85:205-214. doi:10.1016/j.catena.2011.01.002.

Alfaro, S. C., Gaudichet, A., Gomes, L., and Maillé, M.: Mineral aerosol production by wind erosion: aerosol particle sizes and binding energies., Geophys. Res. Lett., 25, 991-994, 1998.

Andreae, M. O., Berresheim, H., Andreae, T. W., Kritz, M. A., Bates, T. S., and Merrill, J. T.: Vertical distribution of dimethylsulfide, sulfur dioxide, aerosol ions, and radon over the Northeast Pacific ocean, J. Atmos. Chem., 6, 149-173, 1988.

Ansmann, A., Petzold, A., Kandler, K., Tegen, I. N. A., Wendisch, M., Mümler, D., Weinzierl, B., Müller, T., and Heintzenberg, J.: Saharan Mineral Dust Experiments SAMUM–1 and SAMUM–2: what have we learned?, Tellus B, 63, 403-429, 10.1111/j.1600-0889.2011.00555.x, 2011.

1037 Arimoto, R., Balsam, W., and Schloesslin, C.: Visible spectroscopy of aerosol
1038 particles collected on filters: iron-oxide minerals, Atmospheric Environment, 36, 89-96, 2002.

1039 Atkinson, J. D., Murray, B. J., Woodhouse, M. T., Whale, T. F., Baustian, K. J.,
1040 Carslaw, K. S., Dobbie, S., O/'Sullivan, D., and Malkin, T. L.: The importance of feldspar for
1041 ice nucleation by mineral dust in mixed-phase clouds, Nature, 498, 355-358,
1042 10.1038/nature12278,http://www.nature.com/nature/journal/v498/n7454/abs/nature12278.ht
1043 ml#supplementary-information, 2013.

1044 Balkanski, Y., Schulz, M., Claquin, T., and Guibert, S.: Reevaluation of Mineral
1045 aerosol radiative forcings suggests a better agreement with satellite and AERONET data,
1046 Atmos. Chem. Phys., 7, 81-95, 10.5194/acp-7-81-2007, 2007.

1047 Baron, P. A., and Willeke, K.: Aerosol measurement: Principles, techniques and
1048 applications, 2nd ed., John Wiley and Sons, New York, 2001.

1049 Barthelmy, D., Mineralogy database. Available at http://www.webmineral.com, 2007.

1050 Bedidi A et Cervelle B., Light scattering by spherical particles with hematite and
1051 goethite like optical properties : Effect of water impregnation. J. Geophys. Res., 98, 11,941-
1052 11,952, 1993.

1053 Ben-Ami, Y., Koren, I., and Altaratz, O.: Patterns of North African dust transport over
1054 the Atlantic: winter vs. summer, based on CALIPSO first year data, Atmos. Chem. Phys., 9,
1055 7867-7875, 10.5194/acp-9-7867-2009, 2009.

1056 Ben-Ami, Y., I. Koren, Y. Rudich, P. Artaxo, S. T. Martin, and M. O. Andreae,
1057 Transport of North African dust from the Bodélé depression to the Amazon Basin: a case
1058 study, Atmos. Chem. Phys., 10, 7533–7544, 2010.

1059 Boucher, O., D. Randall, P. Artaxo, C. Bretherton, G. Feingold, P. Forster, V.-M.
1060 Kerminen, Y. Kondo, H. Liao, U. Lohmann, P. Rasch, S.K. Satheesh, S. Sherwood, B.
1061 Stevens and X.Y. Zhang, 2013: Clouds and Aerosols. In: Climate Change 2013: The
1062 Physical Science Basis. Contribution of Working Group I to the Fifth Assessment Report of
1063 the Intergovernmental Panel on Climate Change [Stocker, T.F., D. Qin, G.-K. Plattner, M.
1064 Tignor, S.K. Allen, J. Boschung, A. Nauels, Y. Xia, V. Bex and P.M. Midgley (eds.)].
1065 Cambridge University Press, Cambridge, United Kingdom and New York, NY, USA.

1066 Bristow, C. S., Drake, N., and Armitage, S.: Deflation in the dustiest place on Earth:
1067 The Bodélé Depression, Chad, Geomorphology, 105, 50-58,
1068 http://dx.doi.org/10.1016/j.geomorph.2007.12.014, 2009.

1069 Brooks, N., and Legrand, M.: Dust variability over North Africa and rainfall in the
1070 Sahel, in: Linking climate change to land surface change, Advances in Global Change
1071 Research, Kluwer Academic Publishers, Dordrecht, 1-25, 2003.

1072 Caquineau, S., M.-C. Magonthier, A. Gaudichet, and Gomes, L.: An improved
1073 procedure for the X-ray diffraction analysis of low-mass atmospheric dust samples, Eur. J.
1074 Mineral., 9, 157- 166, 1997.

1075 Caquineau, S., Gaudichet, A., Gomes, L., and Legrand, M.: Mineralogy of Saharan
1076 dust transported over northwestern tropical Atlantic Ocean in relation to source regions, J.
1077 Geophys. Res., 107, 4251, 10.1029/2000jd000247, 2002.

1078 Carslaw, K. S., Boucher, O., Spracklen, D. V., Mann, G. W., Rae, J. G. L., Woodward,
1079 S., and Kulmala, M.: A review of natural aerosol interactions and feedbacks within the Earth
1080 system, Atmos. Chem. Phys., 10, 1701-1737, doi:10.5194/acp-10-1701-2010, 2010.

1081 Chatenet, B., B. Marticorena, L. Gomes, and G. Bergametti, Assessing the microped
1082 size distributions of desert soils erodible by wind, Sedimentology, 43, 901, 1996.

1083 Chou, C., Formenti, P., Maille, M., Ausset, P., Helas, G., Harrison, M., and Osborne,
1084 S.: Size distribution, shape, and composition of mineral dust aerosols collected during the

1085 African Monsoon Multidisciplinary Analysis Special Observation Period 0: Dust and Biomass-
1086 Burning Experiment field campaign in Niger, January 2006, J. Geophys. Res., 113, D00C10,
1087 10.1029/2008jd009897, 2008.

1088 Christidis, G. E., Genesis and compositional heterogeneity of smectites. Part III:
1089 Alteration of basic pyroclastic rocks—A case study from the Troodos Ophiolite Complex,
1090 Cyprus, American Mineralogist, Volume 91, pages 685–701, 2006

1091 Christidis, G. E. and Dunham, A.C., Compositional variations in smectites: Part I.
1092 Alteration of intermediate volcanic rocks. A case study from Milos Island, Greece. Clay
1093 Minerals, 28, 255–273, 1993.

1094 Claquin, T., Schulz, M., and Balkanski, Y. J.: Modeling the mineralogy of atmospheric
1095 dust sources., J. Geophys. Res., 104, 22243-22256, 1999.

1096 Crowley, J. N., Ammann, M., Cox, R. A., Hynes, R. G., Jenkin, M. E., Mellouki, A.,
1097 Rossi, M. J., Troe, J., and Wallington, T. J.: Evaluated kinetic and photochemical data for
1098 atmospheric chemistry: Volume V: heterogeneous reactions on solid substrates, Atmos.
1099 Chem. Phys., 10, 9059-9223, 10.5194/acp-10-9059-2010, 2010.

1100 Cullen, M. J. P., The unified forecast/climate model. Meteorol. Mag. 122: 81–93,
1101 1993.

1102 Dai, A.: Drought under global warming: a review, Wiley Interdisciplinary Reviews:
1103 Climate Change, 2, 45-65, 10.1002/wcc.81, 2011.

1104 Delany, A. C., A. C. Delany, D. W. Parkin, J. J. Griffin, E.D. Goldberg and B.E.F.
1105 Reinmann, Airborne dust collected at Barbados, Geochim. Cosmochim. Acta, 885-909; 1967.

1106 De Souza-Machado, S., L. L. Strow, H. Motteler, and S. Hannon, Infrared dust
1107 spectral signatures from AIRS, Geophys. Res. Lett., 33, doi:10.1029/2005GL024364, 2006.

1108 Dolcater, D. L., J. K. Syers and M. L. Jackson, Titanium as free oxide and substituted
1109 forms in kaolinites and other soil minerals, Clays and Clay Minerals, 18, 71-79, 1970.

1110 ECA (Economic Commission for Africa), Assessing sustainable development in
1111 Africa. Africa's Sustainable Development Bulletin. Economic Commission for Africa, Addis
1112 Ababa, 59 pp., 2005.

1113 Egan, W. G., and Hilgeman, T. W., Optical Properties of Inhomogeneous Materials:
1114 Applications to Geology. Astronomy, Chemistry, and Engineering, Academic Press. 235 pp.
1115 1979.

1116 Flamant, C., Lavaysse, C., Todd, M. C., Chaboureau, J. P., and Pelon, J.: Multi-
1117 platform observations of a springtime case of Bodélé and Sudan dust emission, transport
1118 and scavenging over West Africa, Quarterly Journal of the Royal Meteorological Society,
1119 135, 413-430, 10.1002/qj.376, 2009.

1120 Formenti, P., Elbert, W., Maenhaut, W., Haywood, J., and Andreae, M. O.: Chemical
1121 composition of mineral dust aerosol during the Saharan Dust Experiment (SHADE) airborne
1122 campaign in the Cape Verde region, September 2000, J. Geophys. Res., 108, 8576,
1123 10.1029/2002jd002648, 2003.

1124 Formenti, P., Rajot, J. L., Desboeufs, K., Caquineau, S., Chevaillier, S., Nava, S.,
1125 Gaudichet, A., Journet, E., Triquet, S., Alfaro, S., Chiari, M., Haywood, J., Coe, H., and
1126 Highwood, E.: Regional variability of the composition of mineral dust from western Africa:
1127 Results from the AMMA SOP0/DABEX and DODO field campaigns, J. Geophys. Res., 113,
1128 D00C13, 10.1029/2008jd009903, 2008.

1129 Formenti, P., Nava, S., Prati, P., Chevaillier, S., Klaver, A., Lafon, S., Mazzei, F.,
1130 Calzolai, G., and Chiari, M.: Self-attenuation artifacts and correction factors of light element
1131 measurements by X-ray analysis: Implication for mineral dust composition studies, J.
1132 Geophys. Res., 115, D01203, 10.1029/2009jd012701, 2010.

1133 Formenti, P., Schütz, L., Balkanski, Y., Desboeufs, K., Ebert, M., Kandler, K., Petzold,
1134 A., Scheuvens, D., Weinbruch, S., and Zhang, D.: Recent progress in understanding physical
1135 and chemical properties of African and Asian mineral dust, Atmos. Chem. Phys., 11, 8231-
1136 8256, 10.5194/acp-11-8231-2011, 2011a.

1137 Formenti, P., Rajot, J. L., Desboeufs, K., Saïd, F., Grand, N., Chevaillier, S., and
1138 Schmechtig, C.: Airborne observations of mineral dust over western Africa in the summer
1139 Monsoon season: spatial and vertical variability of physico-chemical and optical properties,
1140 Atmos. Chem. Phys., 11, 6387-6410, 10.5194/acp-11-6387-2011, 2011b.

1141 Gillette, D., and T. R. Walker, Characteristics of airborne particles produced by wind
1142 erosion of sandy soil, high plains of West Texas, Soil Sci., 123, 97-110, 1977.

1143 Ginoux, P., J. M. Prospero, T. E. Gill, N. C. Hsu, and M. Zhao (2012), Global-scale
1144 attribution of anthropogenic and natural dust sources and their emission rates based on
1145 MODIS Deep Blue aerosol products, Rev. Geophys., 50, RG3005,
1146 doi:10.1029/2012RG000388.

1147 Glaccum, R. A. and J. M. Prospero, Saharan aerosols over the tropical north Atlantic -
1148 mineralogy. Marine Geology, 37, 295-321, 1980.

1149 Glotch TD, Rossman GR, Aharonson O. 2007. Mid-infrared (5–100 μm) reflectance
1150 spectra and optical constants of ten phyllosilicate minerals. Icarus. 192 : 604–622.
1151 DOI:10.1016/j.icarus.2007.07.002.

1152 Glotch TD et Rossman GR., Mid-infrared reflectance spectra and optical constants of
1153 six iron oxide/oxyhydroxide phases. Icarus 204, 663–671, 2009.

1154 Goudie, A. S., and Middleton, N. J.: Saharan dust storms: nature and consequences,
1155 Earth-Science Reviews 56, 179-204, 2001.

1156 Gustafsson, R. J., A. Orlov, P. T. Griffiths, R. A. Cox, and R. M. Lambert, Reduction
1157 of NO_2 to nitrous acid on illuminated titanium dioxide aerosol surfaces: implications for
1158 photocatalysis and atmospheric chemistry, Chem. Commun., 1359–7345, 3936–3938, 2006.

1159 Hansell, Jr., R. A., Reid, J. S., Tsay, S. C., Roush, T. L., and Kalashnikova, O. V., A
1160 sensitivity study on the effects of particle chemistry, asphericity and size on the mass
1161 extinction efficiency of mineral dust in the earth's atmosphere: from the near to thermal IR,
1162 Atmos. Chem. Phys., 11, 1527-1547, doi:10.5194/acp-11-1527-2011, 2011.

1163 Haywood, J. M., R. P. Allan, I. Culverwell, T. Slingo, S. Milton, J. Edwards, and N.
1164 Clerbaux, Can desert dust explain the outgoing longwave radiation anomaly over the Sahara
1165 during July 2003?, J. Geophys. Res., 110, D05105, doi:10.1029/2004JD005232, 2005.

1166 Haywood, J. M., Pelon, J., Formenti, P., Bharmal, N., Brooks, M., Capes, G.,
1167 Chazette, P., Chou, C., Christopher, S., Coe, H., Cuesta, J., Derimian, Y., Desboeufs, K.,
1168 Greed, G., Harrison, M., Heese, B., Highwood, E. J., Johnson, B., Mallet, M., Marticorena,
1169 B., Marsham, J., Milton, S., Myhre, G., Osborne, S. R., Parker, D. J., Rajot, J. L., Schulz, M.,
1170 Slingo, A., Tanré, D., and Tulet, P.: Overview of the Dust and Biomass-burning Experiment
1171 and African Monsoon Multidisciplinary Analysis Special Observing Period-0, J. Geophys.
1172 Res., 113, D00C17, 10.1029/2008jd010077, 2008.

1173 Haywood, J. M., Johnson, B. T., Osborne, S. R., Baran, A. J., Brooks, M., Milton, S.
1174 F., Mulcahy, J., Walters, D., Allan, R. P., Klaver, A., Formenti, P., Brindley, H. E.,
1175 Christopher, S., and Gupta, P.: Motivation, rationale and key results from the GERBILS
1176 Saharan dust measurement campaign, Quarterly Journal of the Royal Meteorological
1177 Society, 137, 1106-1116, 10.1002/qj.797, 2011.

1178 Heintzenberg, J., The SAMUM-1 experiment over Southern Morocco: overview and
1179 introduction. Tellus 61B, doi:10.1111/j.1600-0889.2008.00403.x, 2008.

Hess, M., Koepke, P., and Schult, I.: Optical properties of aerosols and clouds: The software package OPAC, Bull. Am. Meteorol. Soc, 79, 831–844, 1998.

Highwood, E. J., J.M. Haywood, M. D. Silverstone, S.M. Newman, and J. P. Taylor, Radiative properties and direct effect of Saharan dust measured by the C-130 aircraft during Saharan Dust Experiment (SHADE): 2. Terrestrial spectrum, J. Geophys. Res., 108(D18), 8578, doi:10.1029/2002JD002552, 2003.

Hinds, W. C.: Aerosol technology: properties, behavior, and measurement of airborne particles, John Wiley & Sons, Chichester, 504 pp., 1999.

Hoose, C U Lohmann1, R Erdin1 and I Tegen, The global influence of dust mineralogical composition on heterogeneous ice nucleation in mixed-phase clouds, 2008 *Environ. Res. Lett.* 3 025003.

Hower, J., and T. C. Mowatt, The Mineralogy of illites and mixed –layer illite/Montmorrilonites, American Mineralogist, 51, 825-854, 1966.

Hudson, P. K., E. R. Gibson, M. A. Young, P. D. Kleiber, and V. H. Grassian, Coupled infrared extinction and size distribution measurements for several clay components of mineral dust aerosol, J. Geophys. Res., 113, D01201, doi:10.1029/2007JD008791, 2008a.

Hudson, P.K., Young, M.A., Kleiber, P.D., Grassian, V.H., coupled infrared extinction spectra and size distribution measurements for several non-clay components of mineral dust aerosol (quartz, calcite, and dolomite). Atmos. Environ. 42, 5991e5999, 2008b.

Huneeus, N., Schulz, M., Balkanski, Y., GrieSFeller, J., Kinne, S., Prospero, J., Bauer, S., Boucher, O., Chin, M., Dentener, F., Diehl, T., Easter, R., Fillmore, D., Ghan, S., Ginoux, P., Grini, A., Horowitz, L., Koch, D., Krol, M. C., Landing, W., Liu, X., Mahowald, N., Miller, R., Morcrette, J. J., Myhre, G., Penner, J. E., Perlwitz, J., Stier, P., Takemura, T., and Zender, C.: Global dust model intercomparison in AeroCom phase I, Atmos. Chem. Phys. Discuss., 10, 23781-23864, 10.5194/acpd-10-23781-2010, 2010.

Janicot, S., Thorncroft, C. D., Ali, A., Asencio, N., Berry, G., Bock, O., Bourles, B., Caniaux, G., Chauvin, F., Deme, A., Kergoat, L., Lafore, J. P., Lavaysse, C., Lebel, T., Marticorena, B., Mounier, F., Nedelec, P., Redelsperger, J. L., Ravegnani, F., Reeves, C. E., Roca, R., de Rosnay, P., Schlager, H., Sultan, B., Tomasini, M., Ulanovsky, A., and team, A. f.: Large-scale overview of the summer monsoon over West Africa during the AMMA field experiment in 2006, Ann. Geophys., 26, 2569-2595, 10.5194/angeo-26-2569-2008, 2008.

Jickells, T. D., An, Z. S., Andersen, K. K., Baker, A. R., Bergametti, G., Brooks, N., Cao, J. J., Boyd, P. W., Duce, R. A., Hunter, K. A., Kawahata, H., Kubilay, N., laRoche, J., Liss, P. S., Mahowald, N., Prospero, J. M., Ridgwell, A. J., Tegen, I., and Torres, R.: Global Iron Connections Between Desert Dust, Ocean Biogeochemistry, and Climate, Science, 308, 67-71, 10.1126/science.1105959, 2005.

Johnson, B. T., Osborne, S. R., Haywood, J. M., and Harrison, M. A. J.: Aircraft measurements of biomass burning aerosol over West Africa during DABEX, J. Geophys. Res., 113, D00C06, 10.1029/2007jd009451, 2008.

Journet, E., Desboeufs, K. V., Caquineau, S., and Colin, J.-L.: Mineralogy as a critical factor of dust iron solubility, Geophys. Res. Lett., 35, L07805, 10.1029/2007gl031589, 2008.

Journet, E., Balkanski, Y., and Harrison, S. P.: A new data set of soil mineralogy for dust-cycle modeling, Atmos. Chem. Phys., 14, 3801-3816, doi:10.5194/acp-14-3801-2014, 2014.

Kandler, K., Schütz, L., Deutscher, C., Ebert, M., Hofmann, H., Jäckel, S., Jaenicke, R., Knippertz, P., Lieke, K., Massling, A., Petzold, A., Schladitz, A., Weinzierl, B., Wiedensohler, A., Zorn, S., and Weinbruch, S.: Size distribution, mass concentration, chemical and mineralogical composition and derived optical parameters of the boundary

1228 layer aerosol at Tinfou, Morocco, during SAMUM 2006, Tellus B, 61, 32-50, 10.1111/j.1600-
1229 0889.2008.00385.x, 2009.

1230 Karickhoff, S. W., and Bailey, G. W.: Optical absorption spectra of clay minerals,
1231 Clays Clay Min., 21, 59-70, 1973.

1232 Kiefert, L., G. H. McTainsh, and W. G. Nickling, Sedimentological characteristics of
1233 Saharan and Australian dust, in The Impact of Desert Dust Across the Mediterranean, edited
1234 by S. Guerzoni and R. Chester, pp.183– 190, Kluwer Acad., Norwell, Mass., 1996.

1235 Klaver, A., Formenti, P., Caquineau, S., Chevaillier, S., Ausset, P., Calzolai, G.,
1236 Osborne, S., Johnson, B., Harrison, M., and Dubovik, O.: Physico-chemical and optical
1237 properties of Sahelian and Saharan mineral dust: in situ measurements during the GERBILS
1238 campaign, Quarterly Journal of the Royal Meteorological Society, 137, 1193-1210,
1239 10.1002/qj.889, 2011.

1240 Klaver, A., Estimation des propriétés optiques des poussières désertiques d'origines
1241 saharienne et sahélienne, à proximité de leurs zones sources d'émission, à partir de leurs
1242 propriétés physico-chimiques, thèse de Doctorat, Université Paris VII, 2012.

1243 Kluser, L. and Schepanski, K.: Remote sensing of mineral dust over land with MSG
1244 infrared channels: a new Bitemporal Mineral Dust Index, Remote Sens. Environ., 113, 1853–
1245 1867, 2009

1246 Klüser, L., Martynenko, D., Holzer-Popp, T., Thermal infrared remote sensing of
1247 mineral dust over land and ocean: a spectral SVD based retrieval approach for IASI. Atmos.
1248 Meas. Tech. 4, 757e773. doi:10.5194/amt-4-757-2011, 2011.

1249 Klüser, L.; Kleiber, P.; Holzer-Popp, T.; Grassian, V. H., Desert Dust Observation
1250 From Space – Application of Measured Mineral Component Infrared Extinction Spectra,
1251 *Atmos. Environ.*, 54, 419-427, 2012.

1252 Köster, H. M., Ehrlicher, U., Gilg, H. A., Jordan, R., Murad, E., and Onnich, K.:
1253 Mineralogical and chemical characteristics of five nontronites and Fe-rich smectites, Clay
1254 Minerals, 34, 579-599, 1999.

1255 Koren, I., Y. J. Kaufman, R. Washington, M. C. Todd, Y. Rudich, J. Vanderlei Martins
1256 and D. Rosenfeld, The Bodélé depression: a single spot in the Sahara that provides most of
1257 the mineral dust to the Amazon forest, Environ. Res. Lett., 1, 014005, doi:10.1088/1748-
1258 9326/1/1/014005, 2006.

1259 Lafon, S., Rajot, J., Alfaro, S., and Gaudichet, A.: Quantification of iron oxides in
1260 desert aerosol., Atmospheric Environment, 38, 1211-1218, 2004.

1261 Lafon, S., Sokolik, I. N., Rajot, J. L., Caquineau, S., and Gaudichet, A.:
1262 Characterization of iron oxides in mineral dust aerosols: Implications for light absorption, J.
1263 Geophys. Res., 111, D21207, 10.1029/2005jd007016, 2006.

1264 Laskina, O., M. A. Young, P. D. Kleiber, and V. H. Grassian (2012), Infrared extinction
1265 spectra of mineral dust aerosol: Single components and complex mixtures, J. Geophys.
1266 Res., 117, D18210, doi:10.1029/2012JD017756.

1267 Laurent, B., Marticorena, B., Bergametti, G., Léon, J. F., and Mahowald, N. M.:
1268 Modeling mineral dust emissions from the Sahara desert using new surface properties and
1269 soil database, J. Geophys. Res., 113, D14218, 10.1029/2007jd009484, 2008.

1270 Lazaro, F. J., Gutiérrez, L., Barrón, V., and Gelado, M. D.: The speciation of iron in
1271 desert dust collected in Gran Canaria (Canary Islands): Combined chemical, magnetic and
1272 optical analysis, Atmospheric Environment, 42, 8987-8996, 2008.

1273 Lebel, T., Parker, D. J., Flamant, C., Bourlès, B., Marticorena, B., Mougin, E.,
1274 Peugeot, C., Diedhiou, A., Haywood, J. M., Ngamini, J. B., Polcher, J., Redelsperger, J. L.,
1275 and Thorncroft, C. D.: The AMMA field campaigns: multiscale and multidisciplinary

observations in the West African region, Quarterly Journal of the Royal Meteorological Society, 136, 8-33, 10.1002/qj.486, 2010.

Legrand, M., N'doumé, C., and Jankowiak, I.: Satellite-derived climatology of the Saharan aerosol., in: Passive Infrared Remote Sensing of Clouds and the Atmosphere II, edited by: Lynch, D. K., SPIE, 127-135, 1994.

Lepple, F. K., and C. J. Brine, Organic constituents in eolian dust and surface sediments from northwest Africa, J. Geophys. Res., 81, 1141–1147, 1976.

Long LL, Querry MR, Bell RJ, Alexander RW. 1993. Optical properties of calcite and gypsum in crystalline and powdered form in the infrared and far-infrared. Infrared Physics. 34 : 191-201.

Longtin DR, Shettle EP, Hummel JR, Pryce JD. 1988. A Wind Dependent Desert Aerosol Model: Radiative Properties. AFGL-TR-88-0112, Air Force Geophysics Laboratory, Hanscom AFB, MA.

Mahowald, N., Aerosol indirect effects on biogeochemistry and climate, Science, 334, 794, doi:10.1126/science.1207374, 2011.

Marra AC, Blanco A, Fonti S, Jurewicz A, Orofino V. 2005. Fine hematite particles of Martian interest: absorption spectra and optical constants. Journal of Physics: Conference Series 6 132–138.

Marticorena, B., and Bergametti, G.: Modeling the atmospheric dust cycle: 1. Design of a soil-derived dust emission scheme, J. Geophys. Res., 100, 16415-16430, 10.1029/95jd00690, 1995.

Marticorena, B., Chatenet, B., Rajot, J. L., Traoré, S., Coulibaly, M., Diallo, A., Koné, I., Maman, A., Ndiaye, T., and Zakou, A.: Temporal variability of mineral dust concentrations over West Africa: analyses of a pluriannual monitoring from the AMMA Sahelian Dust Transect, Atmos. Chem. Phys., 10, 8899-8915, 10.5194/acp-10-8899-2010, 2010.

Mason, B.: Principles of Geochemistry, 3rd ed. ed., John Wiley, New York, 1966.

Majestic, B. J., Schauer, J. J., and Shafer, M. M.: Application of synchrotron radiation for measurement of iron red-ox speciation in atmospherically processed aerosols, Atmos. Chem. Phys., 7, 2475-2487, doi:10.5194/acp-7-2475-2007, 2007.

McConnell, C. L., Highwood, E. J., Coe, H., Formenti, P., Anderson, B., Osborne, S., Nava, S., Desboeufs, K., Chen, G., and Harrison, M. A. J.: Seasonal variations of the physical and optical characteristics of Saharan dust: Results from the Dust Outflow and Deposition to the Ocean (DODO) experiment, J. Geophys. Res., 113, D14S05, 10.1029/2007jd009606, 2008.

McConnell, C. L., Formenti, P., Highwood, E. J., and Harrison, M. A. J.: Using aircraft measurements to determine the refractive index of Saharan dust during the DODO Experiments, Atmos. Chem. Phys., 10, 3081-3098, 10.5194/acp-10-3081-2010, 2010.

Mehra, O. P., and Jackson, M. L.: Iron oxide removal from soils and clays by a dithionite-citrate buffered with sodium bicarbonate, Clay Minerals, 7, 317-327, 1960.

Mestdagh, M. M., L. Vielvoye and A.J. Herbillon, Iron in Kaolinite: The relationship between kaolinite crystallinity and iron content, Clay Minerals, 15, 1-13, 1980.

Mogili, P. K., Yang, K. H., Young, M. A., Kleiber, P. D., and Grassian, V. H.: Environmental aerosol chamber studies of extinction spectra of mineral dust aerosol components: Broadband IR-UV extinction spectra, Journal of Geophysical Research: Atmospheres, 112, D21204, 10.1029/2007jd008890, 2007.

Mogili, P. K., Yang, K. H., Young, M. A., Kleiber, P. D., and Grassian, V. H.: Extinction spectra of mineral dust aerosol components in an environmental aerosol chamber: IR

resonance studies, Atmospheric Environment, 42, 1752-1761, http://dx.doi.org/10.1016/j.atmosenv.2007.11.026, 2008.

Mooney, T., and R. F. Knacke, Optical Constants of Chlorite and Serpentine between 2.5 and 50 μm, ICARUS, 64, 493-502, 1985.

Müller, T., Schladitz, A., Massling, A., Kaaden, N., Kandler, K., and Wiedensohler, A.: Spectral absorption coefficients and imaginary parts of refractive indices of Saharan dust during SAMUM-1, Tellus B, 61, 79-95, 10.1111/j.1600-0889.2008.00399.x, 2009.

Murad, E. and Wagner, U., The Mossbauer spectrum of illite, Clay Minerals, 29, 1-10, 1994.

Ndour, M., B. D'Anna, C. George, O. Ka, Y. Balkanski, J. Kleffmann, K. Stemmler, and M. Ammann, Photoenhanced uptake of NO_2 on mineral dust: Laboratory experiments and model simulations, Geophys. Res. Lett., 35, doi:10.1029/2007GL032006., 2008.

Nickovic, S., Vukovic, A., Vujadinovic, M., Djurdjevic, V., and Pejanovic, G., Technical Note: High-resolution mineralogical database of dust-productive soils for atmospheric dust modeling, Atmos. Chem. Phys., 12, 845-855, doi:10.5194/acp-12-845-2012, 2012.

N'Tchayi, G. M., Bertrand, J., Legrand, M., and Baudet, J.: Temporal and spatial variations of the atmospheric dust loading throughout West Africa over the last thirty years, Ann. Geophys., 12, 265-273, doi:10.1007/s00585-994-0265-3, 1994.

N'Tchayi Mbourou, G., Bertrand, J., and Nicholson, S. E.: The diurnal and seasonal cycles of wind-borne dust over Africa north of the equator, J. Appl. Meteor., 36, 868-882, 1997.

O'Day, P. A., Rivera, N., Root, R., and Carroll, S. A.: X-ray absorption spectroscopic study of Fe reference compounds for the analysis of natural sediments, American Mineralogist, 89, 572-585, 2004.

Ohta, A., Tsuno, H., Kagi, H., Kanai, Y., Nomura, M., Zhang, R., Terashima, N., and Imai, N.: Chemical compositions and XANES speciations of Fe, Mn and Zn from aerosols collected in China and Japan during dust events, Geochemical Journal, 40, 363-376, 2006.

Paquet, H., Coudé-Gaussen, G., and Rognon, P.: Etude minéralogique de poussières sahariennes le long d'un itinéraire entre 19° et 35° de latitude nord, Révue de Géologie Dynamique et de Géographie Physique, 25, 257-265, 1984.

Paris, R., Desboeufs, K. V., and Journet, E.: Variability of dust iron solubility in atmospheric waters: Investigation of the role of oxalate organic complexation, Atmospheric Environment, 45, 6510-6517, http://dx.doi.org/10.1016/j.atmosenv.2011.08.068, 2011.

Patterson, E., Gillette, D., and Stockton, B.: Complex index of refraction between 300 and 700 nm for Saharan aerosols, J. Geophys. Res., 82, 3153-3160, 1977.

Pentrakova, L., SU, K., Pentak, M., and J. W. Stucki, A review of microbial redox interactions with structural Fe in clay minerals, Clay Minerals, 48, 543–560, 2013.

Peterson JT et Weinman JA. 1969. Optical properties of quartz dust particles at infrared wavelengths. Journal of Geophysical Research Letters. 74 : 6947-6952.

Prietzel, J., Thieme, J., Eusterhues, K., and Eichert, D.: Iron speciation in soils and soil aggregates by synchrotron-based x. ray microspectroscopy (xanes, mu-xanes), Eur. J. Soil. Sci., 58, 1027–1041, 2007.

Prospero, J. M., Ginoux, P., Torres, O., Nicholson, S. E., and Gill, T. E.: Environmental characterization of global sources of atmospheric soil dust identified with the Nimbus 7 Total Ozone Mapping Spectrometer (TOMS) absorbing aerosol product., Rev. Geophys., 40, 2-1 to 2-31, 2002.

Pye, K.: Aeolian Dust and Dust Deposits, Academic Press, London, 334 pp., 1987.

1370 Querry MR, Osborne G, Lies K, Jordon R, Coveney RM. 1978. Complex refractive
1371 index of limestone in the visible and infrared. Applied Optics. 17 : 353–356.

1372 Querry MR. 1987. Optical constants of minerals and other materials from the
1373 millimeter to the UV. U.S. Army Rep. CRDEC-CR- 88009, Aberdeen, MD.

1374 Rahn, K. A.: Silicon and aluminum in atmospheric aerosols: crust-air fractionation?,
1375 Atmos. Environ., 10, 597-601, 1976.

1376 Rajot, J.-L.: Wind blown sediment mass budget of Sahelian village land units in
1377 Niger., Bull. Soc. Géol. France, 172, 523-531, 2001.

1378 Rajot, J. L., Formenti, P., Alfaro, S., Desboeufs, K., Chevaillier, S., Chatenet, B.,
1379 Gaudichet, A., Journet, E., Marticorena, B., Triquet, S., Maman, A., Mouget, N., and Zakou,
1380 A.: AMMA dust experiment: An overview of measurements performed during the dry season
1381 special observation period (SOP0) at the Banizoumbou (Niger) supersite, J. Geophys. Res.,
1382 113, D00C14, 10.1029/2008jd009906, 2008.

1383 Redelsperger, J.-L., Thorncroft, C. D., Diedhiou, A., Lebel, T., Parker, D. J., and
1384 Polcher, J.: African Monsoon Multidisciplinary Analysis: An International Research Project
1385 and Field Campaign, Bulletin of the American Meteorological Society, 87, 1739-1746,
1386 doi:10.1175/BAMS-87-12-1739, 2006.

1387 Reeves, C. E., Formenti, P., Afif, C., Ancellet, G., Attié, J. L., Bechara, J., Borbon, A.,
1388 Cairo, F., Coe, H., Crumeyrolle, S., Fierli, F., Flamant, C., Gomes, L., Hamburger, T.,
1389 Jambert, C., Law, K. S., Mari, C., Jones, R. L., Matsuki, A., Mead, M. I., Methven, J., Mills, G.
1390 P., Minikin, A., Murphy, J. G., Nielsen, J. K., Oram, D. E., Parker, D. J., Richter, A., Schlager,
1391 H., Schwarzenboeck, A., and Thouret, V.: Chemical and aerosol characterisation of the
1392 troposphere over West Africa during the monsoon period as part of AMMA, Atmos. Chem.
1393 Phys., 10, 7575-7601, 10.5194/acp-10-7575-2010, 2010.

1394 Reid, E. A., Reid, J. S., Meier, M. M., Dunlap, M. R., Cliff, S. S., Broumas, A., Perry,
1395 K., and Maring, H.: Characterization of African dust transported to Puerto Rico by individual
1396 particle and size segregated bulk analysis, J. Geophys. Res., 108, 8591,
1397 10.1029/2002jd002935, 2003.

1398 Saïd, F., Canut, G., Durand, P., Lohou, F., and Lothon, M.: Seasonal evolution of
1399 boundary-layer turbulence measured by aircraft during the AMMA 2006 Special Observation
1400 Period, Quarterly Journal of the Royal Meteorological Society, 136, 47-65, 10.1002/qj.475,
1401 2010.

1402 Schepanski, K., I. Tegen, B. Laurent, B. Heinold, and A. Macke, A new Saharan dust
1403 source activation frequency map derived from MSG-SEVIRI IR channels, Geophys. Res.
1404 Lett., 34, L18803, doi:10.1029/ 2007GL030168, 2007.

1405 Schepanski, K., Tegen, I., Todd, M. C., Heinold, B., Bönisch, G., Laurent, B., and
1406 Macke, A.: Meteorological processes forcing Saharan dust emission inferred from MSG-
1407 SEVIRI observations of subdaily dust source activation and numerical models, J. Geophys.
1408 Res., 114, D10201, 10.1029/2008jd010325, 2009.

1409 Schepanski, K., I. Tegen, A. Macke, Comparison of satellite based observations of
1410 Saharan dust source areas, Remote Sensing of Environment, 123, 90–97, 2012.

1411 Scheuvens, D., Schütz, L., Kandler, K., Ebert, M., and (2007), Weinbruch, S.: Bulk
1412 composition of northern African dust and its source sediments — A compilation, Earth-
1413 Science Reviews, 116, 170-194, http://dx.doi.org/10.1016/j.earscirev.2012.08.005, 2013.

1414 Smith A. J. A. and Grainger, R. G., Does variation in mineral composition alter the
1415 short-wave light scattering properties of desert dust aerosol? J. Quant. Spectrosc. Radiat.
1416 Transfer, http://dx.doi.org/10.1016/j. jqsrt.2013.08.005i, 2013.

1417 Schroth, A. W., Crusius, J., Sholkovitz, E. R., and Bostick, B. C.: Iron solubility driven
1418 by speciation in dust sources to the ocean, Nature Geosci., 2, 337-340, 2009.

1419 Shao, Y., Wyrwoll, K.-H., Chappell, A., Huang, J., Lin, Z., McTainsh, G. H., Mikami,
1420 M., Tanaka, T. Y., Wang, X., and Yoon, S.: Dust cycle: An emerging core theme in Earth
1421 system science, Aeolian Research, 2, 181-204,
1422 http://dx.doi.org/10.1016/j.aeolia.2011.02.001, 2011.

1423 Shettle, E. P. and Fenn, R. W., Models for the Aerosols of the Lower Atmosphere and
1424 the Effects of Humidity Variations on Their Optical Properties. AFGL-TR-79-0214,
1425 ADA085951, 1979.

1426 Shi, Z., et al. (2011), Influence of chemical weathering and aging of iron oxides on the
1427 potential iron solubility of Saharan dust during simulated atmospheric processing, Global
1428 Biogeochem. Cycles, 25, GB2010, doi:10.1029/2010GB003837.

1429 Shi, Z., Michael D. Krom, Timothy D. Jickells, Steeve Bonneville, Kenneth S. Carslaw,
1430 Nikos Mihalopoulos, Alex R. Baker, Liane G. Benning, Impacts on iron solubility in the
1431 mineral dust by processes in the source region and the atmosphere: A review, Aeolian
1432 Research, Volume 5, August 2012, Pages 21-42

1433 Sokolik, I. N., Toon, O. B., Bergstrom, R. W., Modeling the radiative characteristics of
1434 airborne mineral aerosols at infrared wavelengths. Journal of Geophysical Research Letters.
1435 103 : 8813-8826, 1998.

1436 Sokolik, I., and Toon, O.: Incorporation of mineralogical composition into models of
1437 the radiative properties of mineral aerosol from UV to IR wavelengths, J. Geophys. Res.,
1438 104, 9423-9444, 1999.

1439 Sokolik, I. N., Winker, D. M., Bergametti, G., Gillette, D. A., Carmichael, G., Kaufman,
1440 Y. J., Gomes, L., Schuetz, L., and Penner, J. E.: Introduction to special section: Outstanding
1441 problems in quantifying the radiative impacts of mineral dust, J. Geophys. Res., 106, 18015-
1442 18027, 10.1029/2000jd900498, 2001.

1443 Sow, M., Alfaro, S. C., Rajot, J. L., and Marticorena, B.: Size resolved dust emission
1444 fluxes measured in Niger during 3 dust storms of the AMMA experiment, Atmos. Chem.
1445 Phys., 9, 3881-3891, 10.5194/acp-9-3881-2009, 2009.

1446 Spitzer WG et Kleinman DA. 1961. Infrared lattice bands of quartz. Physical Review.
1447 121 : 1324-1335.

1448 Tegen, I., and Fung, I.: Modeling of mineral dust in the atmosphere: Sources,
1449 transport, and optical thickness., J. Geophys. Res., 99, 22897-22914, 1994.

1450 Toon, O. B., Pollock, J. B., Khare, B. N., The optical constants of several atmospheric
1451 aerosols species: ammonium sulfate, aluminum oxide and sodium chloride, Journal of
1452 Geophysical Research Letters. 81, 5733-5748, 1976.

1453 Tulet, P., Mallet, M., Pont, V., Pelon, J. and Boone, A., The 7-13 March 2006 dust
1454 storm over West Africa: Generation, transport, and vertical stratification, J. Geophys. Res.,
1455 113, doi: 10.1029/2008JD009871, 2008.

1456 Washington, R., Todd, M., Middleton, N. J., and Goudie, A. S., Dust-storm source
1457 areas determined by the total ozone monitoring spectrometer and surface observations.
1458 Annals of the Association of American Geographers, 93(2), 297–313, 2003.

1459 Washington, R., Todd, M. C., Engelstaedter, S., Mbainayel, S., and Mitchell, F.: Dust
1460 and the low-level circulation over the Bodélé Depression, Chad: Observations from BoDEx
1461 2005, J. Geophys. Res., 111, D03201, 10.1029/2005jd006502, 2006.

1462 Washington, R., Flamant, C., Parker, D. J., Marsham, J., McQuaid, J. B., Brindley, H.,
1463 Todd, M., Highwood, E. J., Chaboureau, J.-P., Kocha, C., Bechir, M., Saci, A., and Ryder, C.
1464 L.: Fennec – The Saharan Climate System, submitted to CLIVAR Exchanges, 2013.

1465 Wilke, M., Farges, F., Petit, P.-E., Brown, G. E. J., and Mertin, F.: Oxidation state and
1466 coordination of Fe in minerals: An Fe K-XANES spectroscopic study, American Mineralogist,
1467 86, 714-730, 2001.

1468 Yoshioka, M., Mahowald, N., Dufresne, J.-L., and Luo, C.: Simulation of absorbing
1469 aerosol indices for African dust, J. Geophys. Res., 110, D18S17, 10.1029/2004jd005276,
1470 2005.

1471

Table captions

Table 1. Calibration coefficients by mineral obtained for the calibration of the XRD analyser used in this study. The calibration coefficients represent the slope of the correlation line between the number of diffracted counts by unit mass. The references of the standard minerals used in this study are also reported.

Table 2. Mean values of the relative proportions of iron in the form of hematite and goethite to total iron oxide as obtained by XAS/XANES analysis. Standard deviations are indicated in parenthesis.

Table 3. Mineralogical composition (percentage by mass, in %) according to the source region. Standard deviations are indicated in parenthesis.

Table 4. Complex refractive indices of individual minerals used in this study. The spectral domains are indicated. *Longtin et al. (1988) have compiled values of complex refractive indices for hematite and quartz based on different sources.

Figure captions

Figure 1. Comparison between the total estimated dust mass (TEDM) estimated from the chemical composition and the total dry gravimetric mass (TDGM) for the AMMA SOP0 (open circles) and AMMA SOP1-2 data (black circles). The dashed line represents the slope of the calculated linear regression.

Figure 2. Geographical identification of the origin of the analysed samples superimposed to the localisation of the major potential source areas (PSA) of mineral dust in western and northern Africa proposed by Formenti et al. (2011a) and Scheuvens et al. (2013) on the basis of the analysis of satellite products and chemical/mineralogical composition on the aerosol and the parent soil. The approximate localisation of the Sahelian dust sources is also indicated by the shed grey area. The location of the Banizoumbou ground-based site is indicated by the black cross. The operating areas of the AMMA, DABEX, DODO and GERBILS field projects are shown. Figure reproduced from Scheuvens et al. (2013) with permission from Elsevier.

Figure 3. Scatterplot of the elemental ratio Fe/Ca versus Si/Al with additional information on source identification based on back-trajectory/satellite and dispersion modeling.

Figure 4. Range of variability of the mineral content (in percent) as obtained by XRD analysis. Boxes indicate the 25, 50 and 75% percentiles. Whiskers indicate the minimum and the maximum values, whereas the open squares indicate the mean value of the distribution.

Figure 5. Variability of the iron oxide content (ratio of Fe_{ox} to total elemental Fe) according to the source region. Boxes indicate the 25, 50 and 75% percentiles. Whiskers indicate the minimum and the maximum values, and points indicate the 5 and 95% percentiles. Data labels are as follows: Mo = Morocco; Ma = Mali; Mau = Mauritania; SA = South Algeria; NN = North Niger. Figure 6. Dependence of the Fe_{ox} content (Fe_{ox}–to–Fe ratio) on the Fe/Ca ratio for samples of different source regions identified in this work.

Figure 7. Scatterplot of the estimated mass of TiO_2 with respect to the total dust mass (TDM). Open circles are used to display values for samples corresponding to transport of Saharan dust, whereas filled circles are for samples corresponding to local emission in the Sahel.

Figure 8. Scatterplot of the Ti/Fe ratio with respect to the Fe_{ox}-to-Fe ratio.

Figure 9. Normalized volume size distribution dV/dlog(EOD) at Banizoumbou during three consequent days in summer (J1 red line, J2 green line, J3 blue line) and one day in winter (black line) for samples representing dust transported from the Bodélé source region. Data are reported as a function of the equivalent optical diameter (EOD) as obtained by optical counter measurements without any corrections for the sample refractive index.

Figure 10. Normalised volume size distribution dV/dlog(EOD) for samples representing dust of emitted dust in the Sahel during episodes local erosions. The explanation of the sample ID is reported in the text.

Figure 11. Imaginary part of the complex refractive index calculated from the mineralogical composition of dust originating from sources PSA5, PSA4, PSA3, local erosion in the Sahel, and PSA2 (from top to bottom). Figure 11.a represents the real part in the 0.3-0.7 μm, calculated assuming refractive index from Table 3. Grey shaded curves represent results obtained when using the data from Bedidi and Cervelle (1993) for hematite, whereas blue shaded areas correspond to using values from Shettle (1979). Figure 11.b represents the imaginary part of the complex refractive index calculated in the 6-16 μm spectral domain. The black line with white diamonds represents data from the OPAC database (Hess et al., 1998).

Figure 12. Iron solubility calculated from the mineralogical composition and from CBD analysis as a function of emission source. Error bars indicate standard deviation. When error bar is not presented, the data is only for one sample.

1536 Table 1. Calibration coefficients by mineral obtained from the calibration of the XRD analyser
1537 used in this study. The calibration coefficients represent the slope of the linear correlation
1538 between the number of diffracted counts by unit mass. The references of the standard
1539 minerals used in this study are also reported. The absolute uncertainty on the slope is also
1540 indicated, whereas numbers in parenthesis are the percent uncertainty obtained as ratio
1541 between the absolute uncertainty and slope value.

Mineral	Origin	Slope (cps mg^{-1})	R^2
Quartz (SiO_2)	Fontainebleau, France	446 ± 14 (3%)	0.88
Calcite ($CaCO_3$)	Bédarieux, France	325 ± 11 (3%)	0.94
Dolomite ($CaMg(CO3)_2$)	Traversella, Italie	679 ± 70 (10%)	0.55
Gypsum ($CaSO_4$ $2H_2O$)	Unknown	446 ± 22 (5%)	0.89
Ortoclase ($KAlSi_3O_8$)	Madagascar	997 ± 70 (7%)	0.69
Albite ($NaAlSi_3O_8$)	Ontario, Canada	2456 ± 56 (2%)	0.96

1542

1543

1544 Table 2. Mean percent values of the oxide fraction of total Fe and relative proportions of
1545 hematite and goethite to total iron oxide as obtained by XAS/XANES analysis. Standard
1546 deviations are indicated in parenthesis.

Origin	Oxide fraction of total Fe (%)	Goethite fraction of Fe oxide (%)	Hematite fraction of Fe oxide (%)
PSA5 (Bodélé)	43 (± 11)	65 (± 7)	35 (± 7)
PSA3 (North Niger)	57 (± 2)	59 (± 8)	41 (± 8)
PSA3 (South Algeria)	55 (---)	62 (---)	38 (---)
Erosion, Sahel	66 (± 5)	68 (± 5)	32 (± 5)

1547 Table 3. Mineralogical composition (percentage by mass, in %) according to the source region. Standard deviations are indicated in parenthesis.

Source	Kaolinite	Illite	Quartz	Ortoclase	Albite	Calcite	Dolomite	Gypsum	Goethite	Hematite	Titanium oxide
Bodélé (wintertime)	84.1 (--)	8.5 (--)	2.9 (--)	0.2 (--)	< DL	0.9 (--)	< DL	0.2 (--)	1.6 (--)	1.1 (--)	0.7
Bodélé/Sudan (summertime)	76.1 (4.4)	7.0 (0.4)	11.2 (5.6)	0.5 (0.2)	0.1 (0.1)	1.3 (0.8)	0.3 (0.1)	0.2 (--)	2.0 (0.3)	1.3 (0.3)	0.7
North Niger/Libya	54.0 (--)	37.8 (--)	4.6 (--)	0.2 (--)	< DL	0.4 (--)	< DL	< DL	1.5 (--)	0.8 (--)	0.8
North Niger/Libya/south Algeria	60.5 (4.7)	24.0 (1.9)	3.6 (3.1)	0.2 (--)	< DL	6.3 (2.9)	< DL	< DL	3.1 (0.2)	1.6 (0.1)	0.8
South Algeria/Mali	71.1 (13.5)	16.4 (11.8)	7.1 (0.8)	0.4 (0.2)	0.2 (0.1)	1.5 (0.01)	0.7 (0.4)	0.3 (--)	1.1 (0.1)	0.8 (0.05)	0.8
South Algeria/North Niger (smectites)	75.2 (3)	7.0 (0.3)	10.8 (2.0)	0.6 (0.2)	0.1 (0.1)	0.9 (0.6)	0.4 (0.2)	0.5 (--)	2.4 (0.6)	1.7 (0.4)	0.8
South Algeria/North Niger (non smectites)	78.2 (2.2)	7.2 (0.2)	6.6 (0.7)	0.4 (0.1)	0.1 (0.02)	3.0 (3.6)	0.2 (0.05)	0.6 (0.3)	2.4 (1.5)	1.8 (1.1)	0.8
North Niger	78.3 (--)	7.4 (--)	9.7 (--)	0.5 (--)	0.1 (--)	< DL	0.3 (--)	0.9 (--)	1.4 (--)	0.7 (--)	0.8
Local erosion (all)	73.0 (13)	7.1 (1.3)	14.3 (13)	0.8 (1)	0.1 (0.2)	< DL	0.1 (--)	0.3 (0.3)	2.1 (0.5)	1.2 (0.4)	1.3
Local erosion (quartz-rich)	46.6 (--)	4.4 (--)	40.6 (--)	2.9 (--)	0.4 (--)	< DL	< DL	< DL	2.4 (--)	1.4 (--)	1.4
Local erosion (excluding quartz-rich)	78.3 (1.5)	7.5 (0.2)	9.1 (2.2)	0.4 (0.1)	< DL	< DL	0.1 (--)	0.3 (0.3)	2.0 (0.6)	1.1 (0.4)	1.4
Mali/Mauritania	29.7 (--)	46.3 (--)	17.3 (--)	1.3 (--)	0.4 (--)	1.0 (--)	0.8 (--)	< DL	1.3 (--)	0.7 (--)x	1.3
Mali/Mauritania/Western Sahara	30.7 (3.2)	54.2 (6.0)	8.4 (1.7)	0.3 (0.1)	0.2 (0.2)	1.2 (0.9)	0.2 (0.2)	0.4 (--)	2.0 (0.5)	1.3 (0.3)	1.3

1548 Table 4. Complex refractive indices of individual minerals used in this study. The spectral
1549 domains are indicated. *Longtin et al. (1988) have compiled values of complex refractive
1550 indices for hematite and quartz based on different sources.

Mineral	Reference	Spectral domain (µm)
Illite	Egan et Hilgeman (1979)	0.185-2.6
	Querry (1987)	2.5-200
	Glotch et al. (2007)	5-100
Kaolinite	Egan et Hilgeman (1979)	0.185-2.6
	Roush et al. (1991)	5-25
	Glotch et al. (2007)	5-100
Calcite	Querry (1978)	0.2-25
	Long et al. (1993)	2.5-300
Dolomite	Barthelmy (2007)	0.185-2.5
	Querry (1987)	2.5-40
Albite	Barthelmy (2007)	0.185-2.5
Ortoclase	Barthelmy (2007)	0.185-2.5
Gypsum	Barthelmy (2007)	0.185-2.5
	Long et al. (1993)	2.5-300
Goethite	Bedidi et Cervelle (1993)	0.46-0.7
	Glotch et Rossman (2009)	8.3-50
Hematite	Bedidi et Cervelle (1993)	0.4-0.7
	Marra et al., (2005)	6.5-50
	Longtin et al. (1988)*	0.2-300
Quartz	Longtin et al.,(1988)*	0.2-2
	Peterson et Weinman (1969)	5-36
	Spitzer et Kleinman (1961)	5-37

1551

1552

1553 Figure 1. Comparison between the total estimated dust mass (TEDM) estimated from the
1554 chemical composition and the total dry gravimetric mass (TDGM) for the AMMA SOP0 (open
1555 circles) and AMMA SOP1-2 data (black circles). The dashed line represents the slope of the
1556 calculated linear regression.

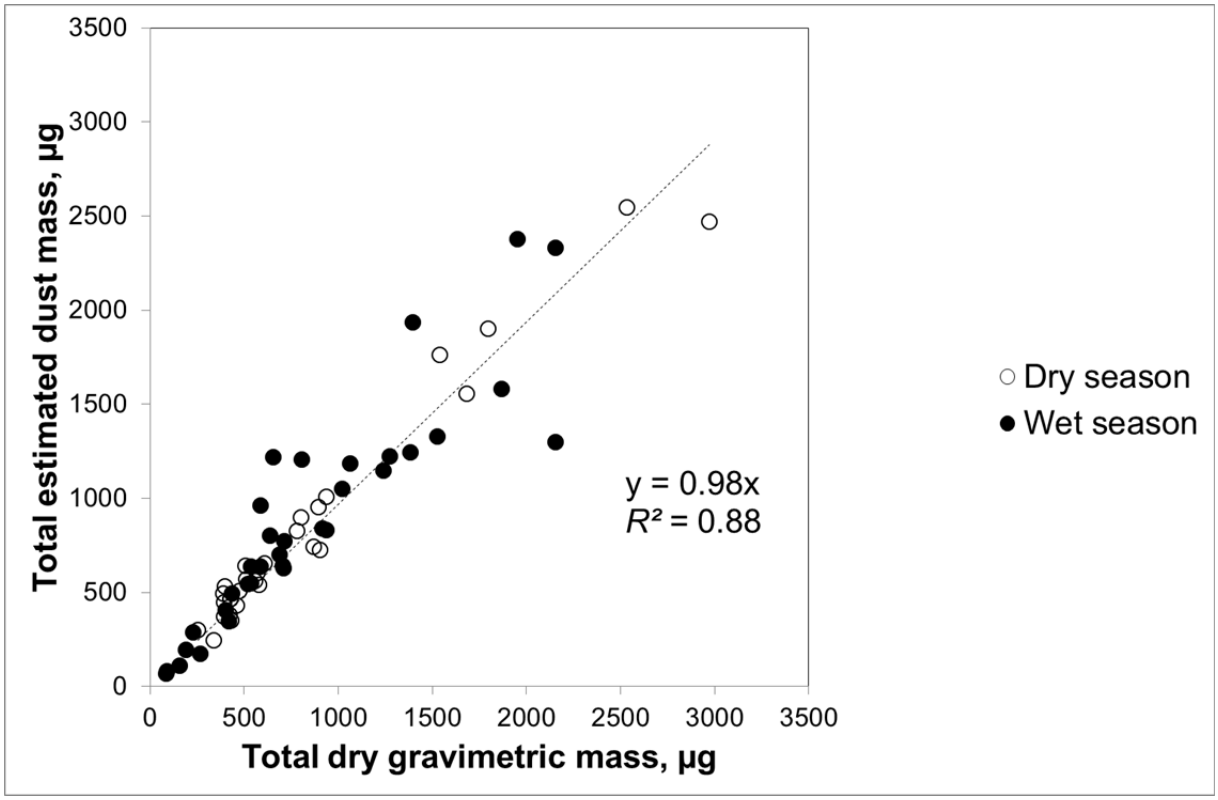

1557

1558

Figure 2. Geographical identification of the origin of the analysed samples superimposed to the localisation of the major potential source areas (PSA) of mineral dust in western and northern Africa proposed by Formenti et al. (2011a) and Scheuvens et al. (2013) on the basis of the analysis of satellite products and chemical/mineralogical composition on the aerosol and the parent soil (Claquin et al., 1999; Brooks and Legrand, 2000; Caquineau et al., 2002; Prospero et al., 2002; Washington et al., 2003; Schepanski et al., 2007; 2009; 2012; Laurent et al., 2008; Klüser and Schepanski, 2009). The approximate localisation of the Sahelian dust sources is also indicated by the shed grey area. The location of the Banizoumbou ground-based site is indicated by the black cross. The operating areas of the AMMA, DABEX, DOD and GERBILS field projects are shown. Figure reproduced from Scheuvens et al. (2013) with permission from Elsevier.

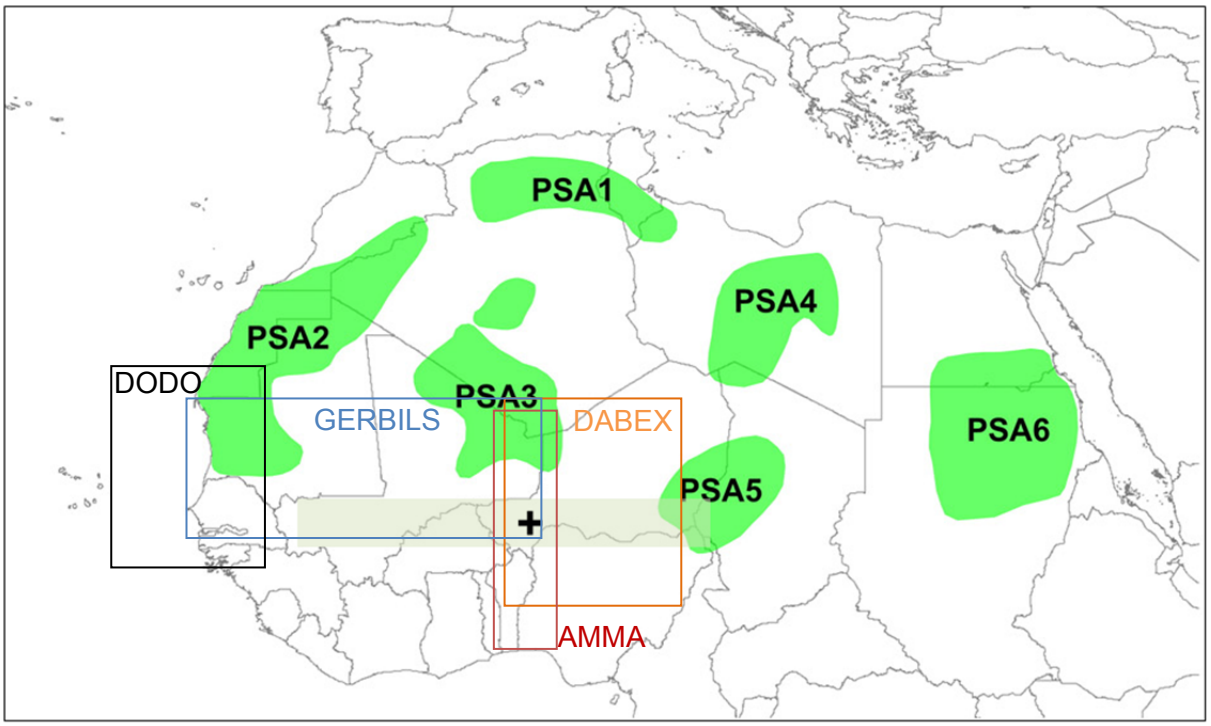

1573 Figure 3. Scatterplot of the elemental ratio Fe/Ca versus Si/Al with additional information on
1574 source identification based on back-trajectory/satellite and dispersion modeling.

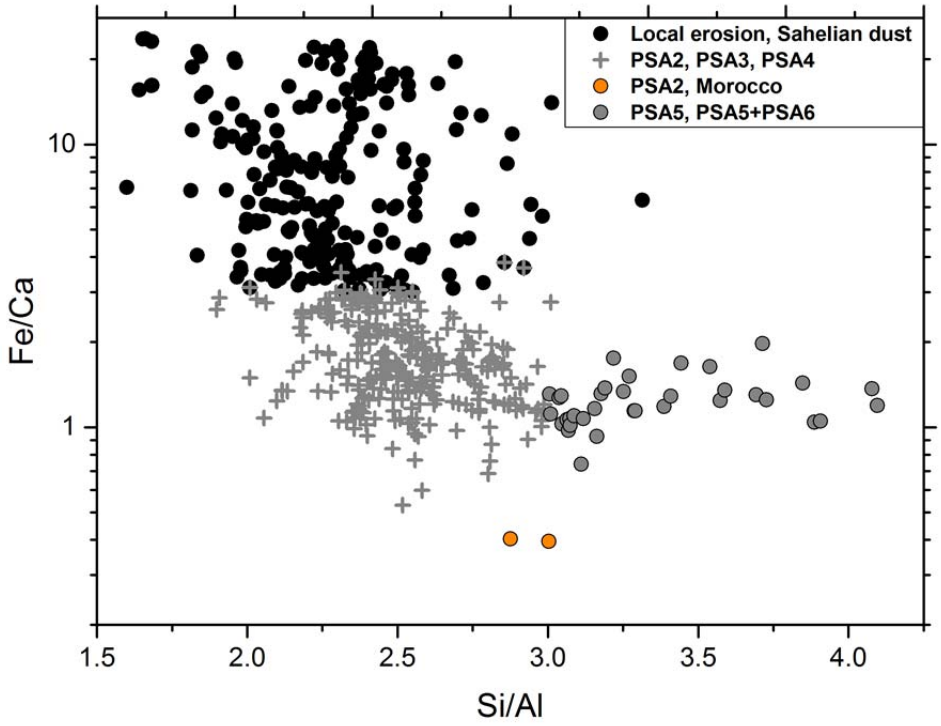

1575
1576

Figure 4. Range of variability of the mineral mass fraction (in percent) as obtained by XRD analysis. Boxes indicate the 25, 50 and 75% percentiles. Whiskers indicate the minimum and the maximum values, whereas the open squares indicate the mean value of the distribution.

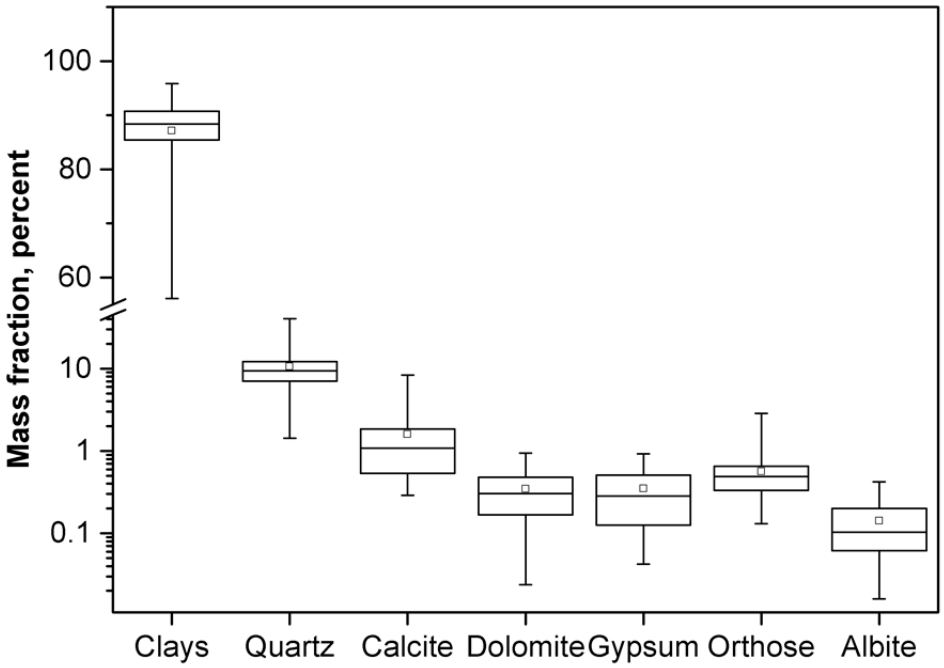

Figure 5. Variability of the iron oxide content (ratio of Fe_{ox} to total elemental Fe) according to the source region. Boxes indicate the 25, 50 and 75% percentiles. Points indicate the minimum and the maximum values, and Whiskers indicate the 5 and 95% percentiles. Data labels are as follows: Mo = Morocco; Ma = Mali; Mau = Mauritania; SA = South Algeria; NN = North Niger.

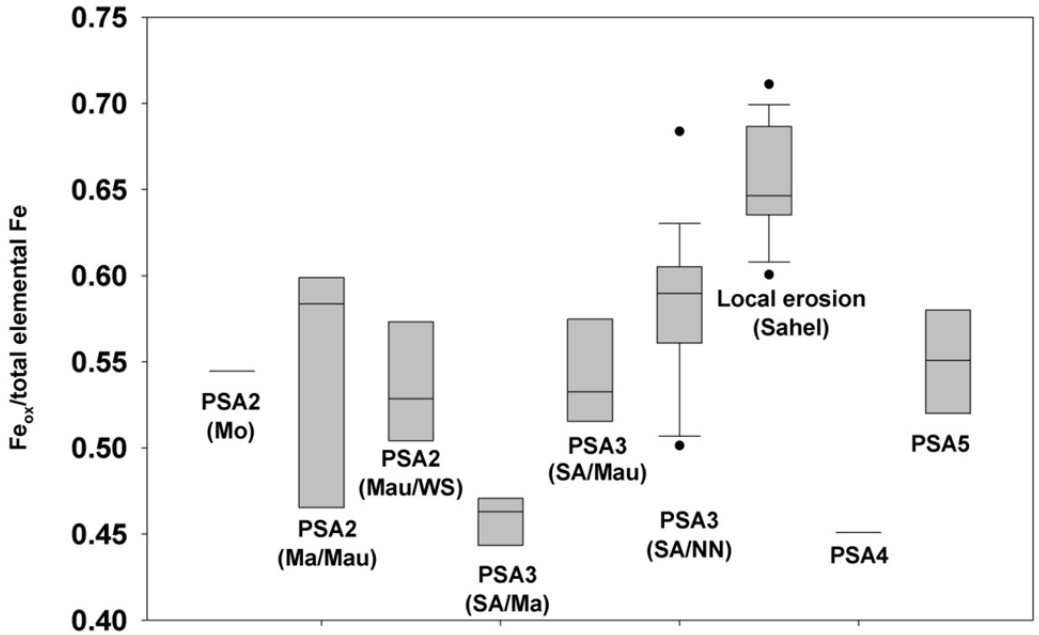

Figure 6. Dependence of the Fe_{ox} content (Fe_{ox}–to–Fe ratio) on the Fe/Ca ratio for samples of different source regions identified in this work.

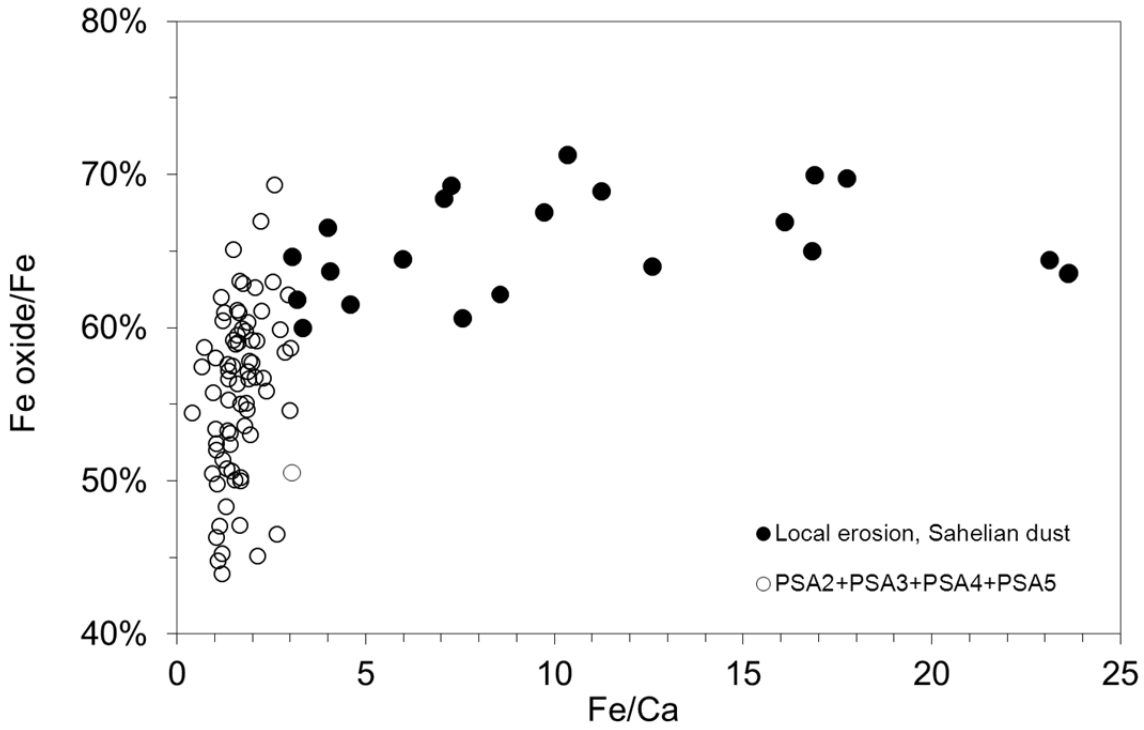

1593 Figure 7. Scatterplot of the estimated mass of TiO_2 with respect to the total dust mass (TDM).
1594 Open circles are used to display values for samples corresponding to transport of Saharan
1595 dust, whereas filled circles are for samples corresponding to local emission in the Sahel.

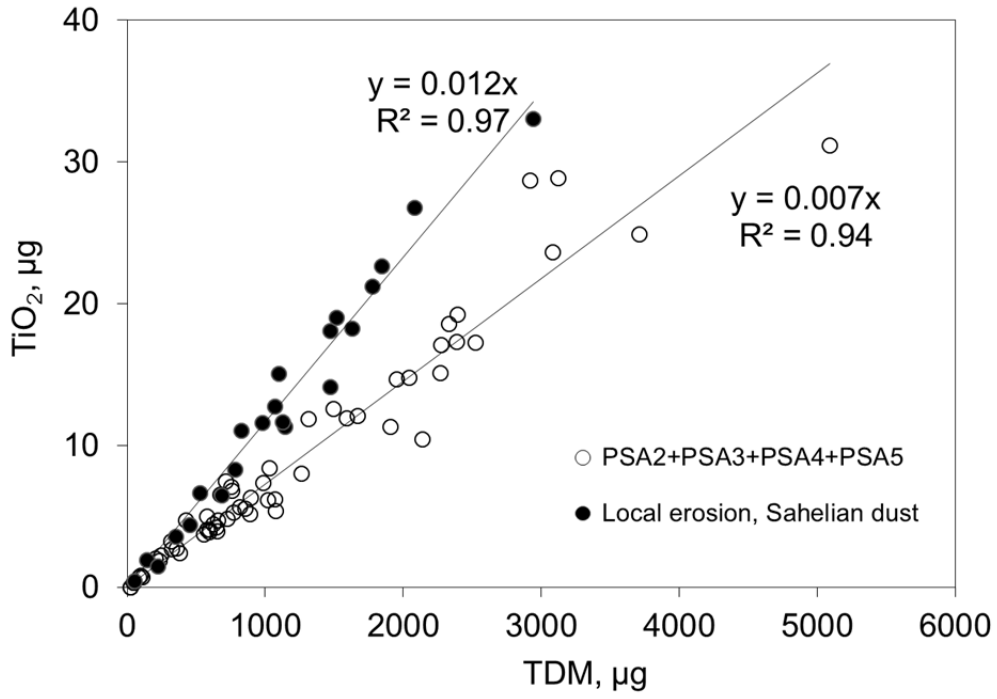

1596

Figure 8. Scatterplot of the Ti/Fe ratio with respect to the Fe_{ox}-to-Fe ratio. Open circles are used to display values for samples corresponding to transport of Saharan dust, whereas filled circles are for samples corresponding to local emission in the Sahel. Two grey points indicates identified mixtures.

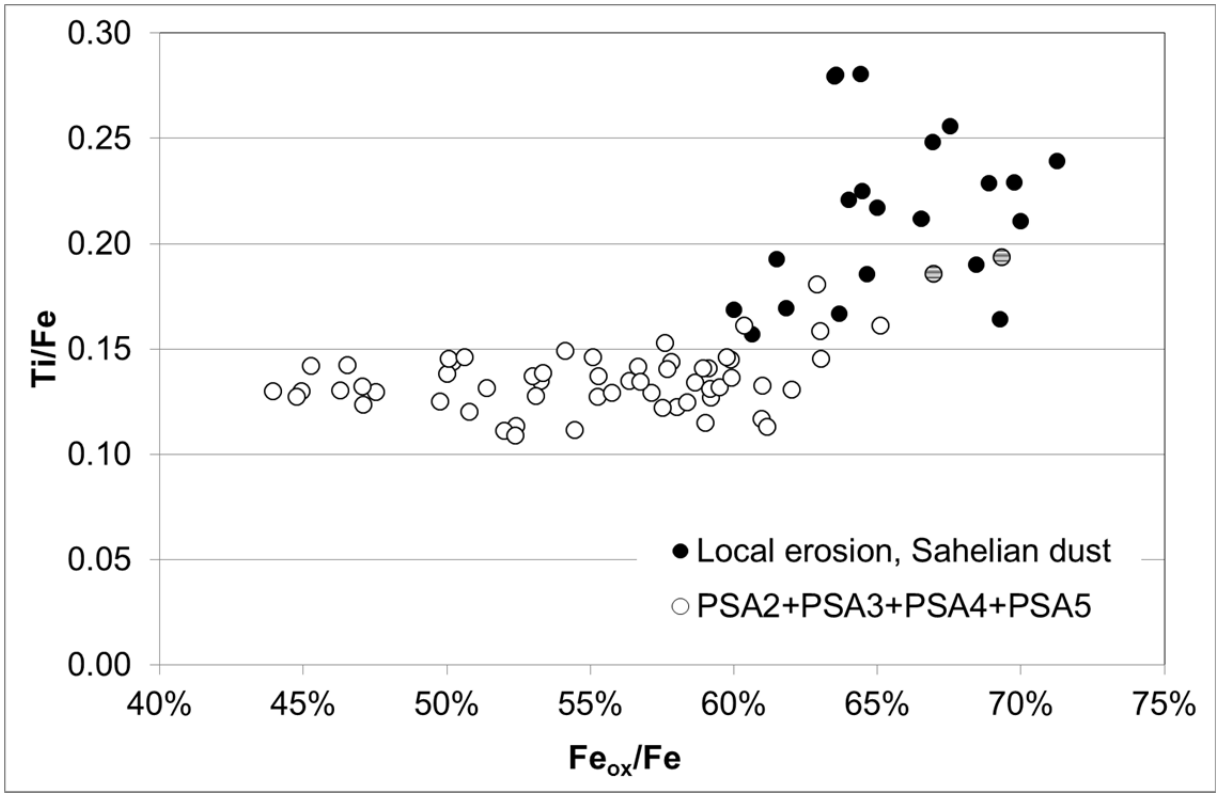

Figure 9. Normalized volume size distribution dV/dlog(EOD) at Banizoumbou during three consequent days in summer (J1 red line, J2 green line, J3 blue line) and one day in winter (black line) for samples representing dust transported from the Bodélé source region. Data are reported as a function of the equivalent optical diameter (EOD) as obtained by optical counter measurements without any corrections for the sample refractive index.

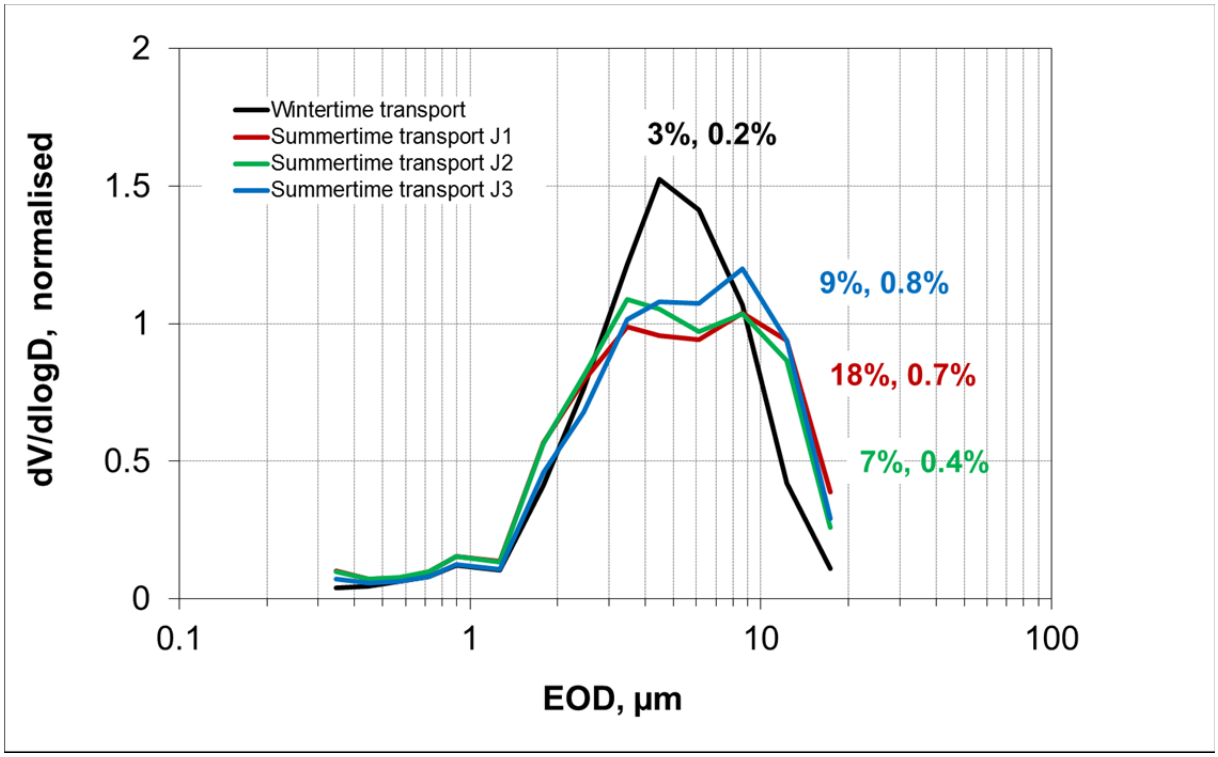

Figure 10. Normalised volume size distribution dV/dlog(EOD) for samples representing Sahelian dust: SOP1-8 representing an episode of local emission by erosion; SOP1-15 and SOP1-60 representing the background dust composition in the absence of local erosion; and SOP1-17 representing the composition of Sahelian dust advected at the sampling site after having been emitted by local erosion in the proximity. Numbers represent the measured percent mass fraction of quartz and feldspars (sum of albite and ortoclase), respectively.

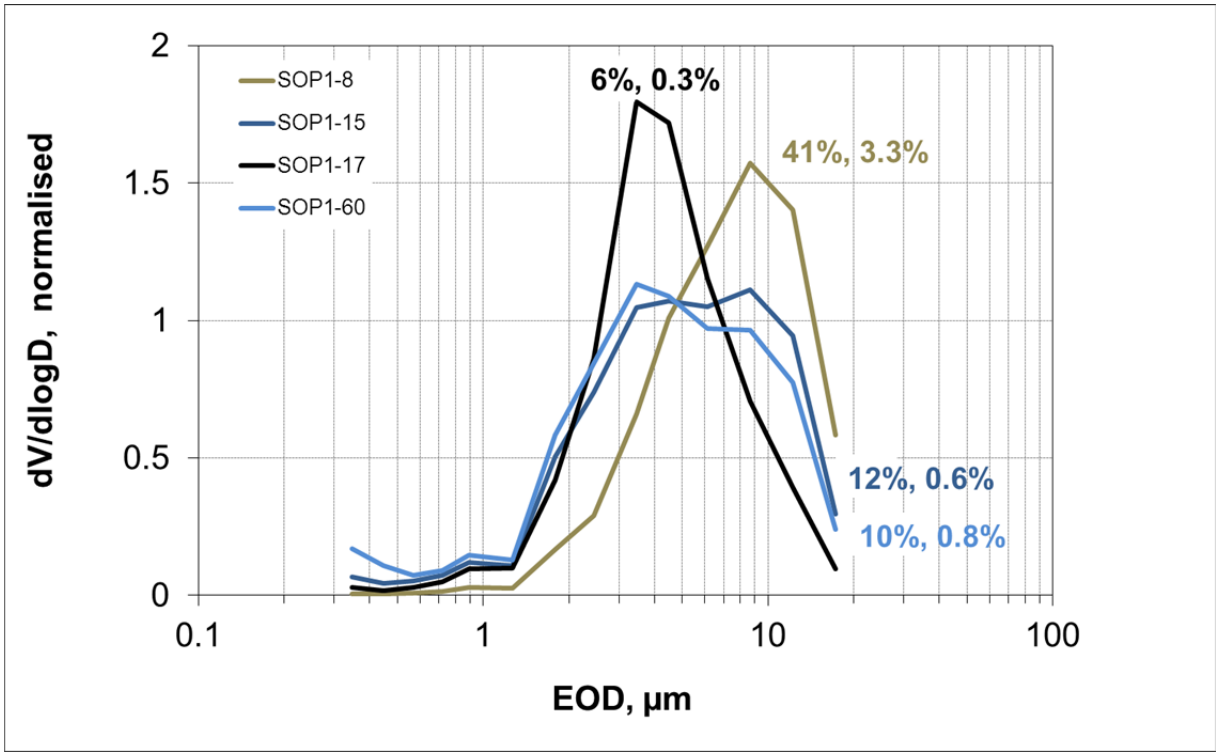

Figure 11. Imaginary part of the complex refractive index calculated from the mineralogical composition of dust steaming from sources PSA5, PSA4, PSA3, local erosion in the Sahel, and PSA2 (from top to bottom). Figure 11.a represents the real part in the 0.3-0.7 µm, calculated assuming refractive index from Table 3. Grey shaded curves represent the mean values (light grey line) and 1 standard deviation (grey shaded areas) obtained when using the data from Bedidi and Cervelle (1993) for hematite, whereas blue shaded areas correspond to values calculated using the hematite data from Shettle (1979). The light blue line represents mean values and the blue shaded area represents one standard deviation. Figure 11.b represents the imaginary part of the complex refractive index calculated in the 6-16 µm spectral domain. The black line with white diamonds represents data from the OPAC database (Hess et al., 1998).

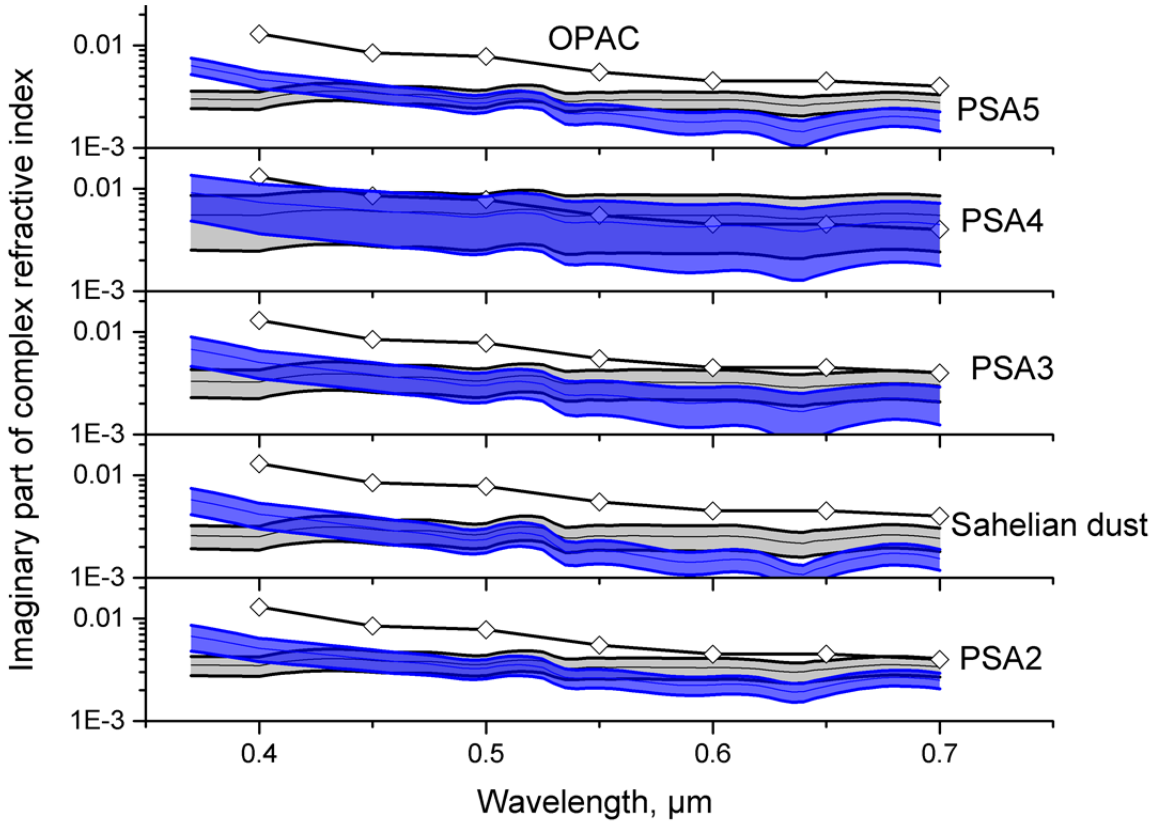

1633 Figure 11. suite

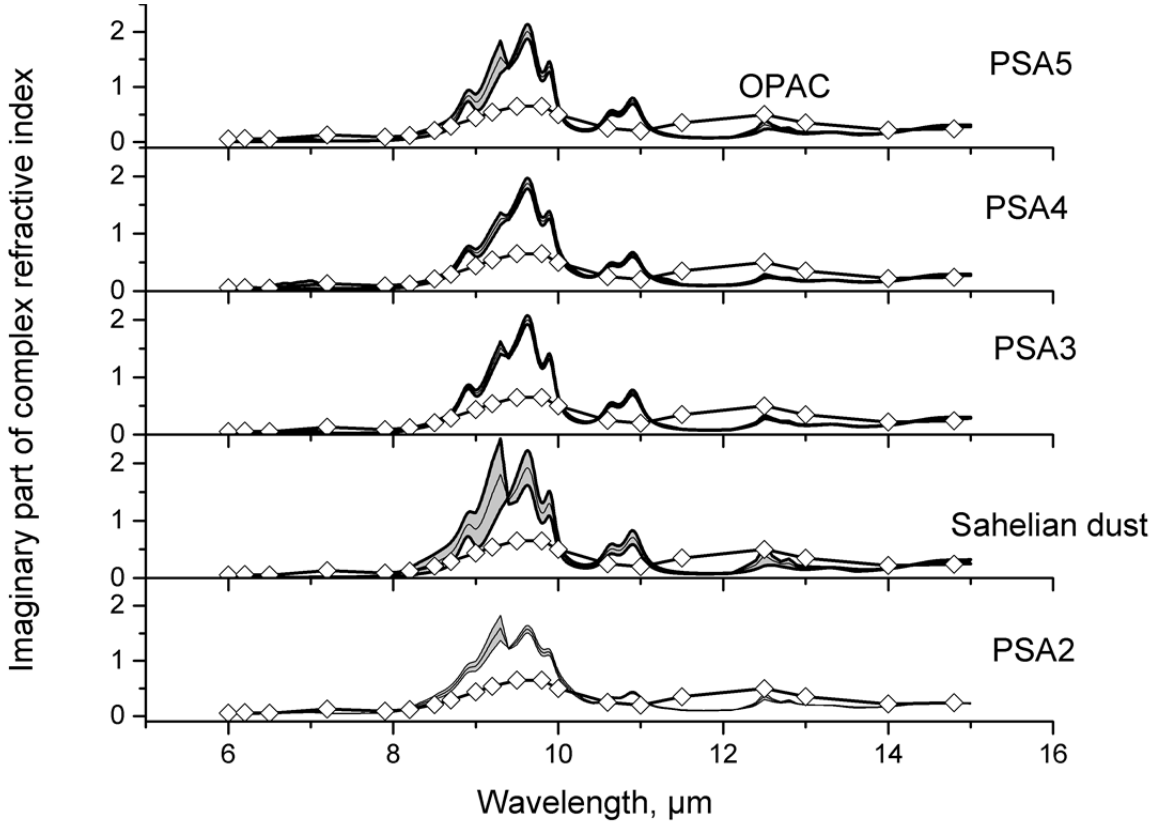

1634

1635

Figure 12. Iron solubility calculated from the mineralogical composition and from CBD analysis as a function of emission source. Error bars indicate standard deviation. When error bar is not presented, the data is only for one sample.